A Practical Theory of Micro-Solar Power Sensor Networks

JAEIN JEONG, Cisco Systems
DAVID CULLER, University of California, Berkeley

Building a micro-solar power system is challenging because it must address long-term system behavior under highly variable solar energy and consider a large design space. We develop a practical theory of micro-solar power systems that is materialized in a simulation suite that models component and system behavior over a long time scale and in an external environment that depends on time, location, weather, and local variations. This simulation provides sufficient accuracy to guide specific design choices in a large design space. Unlike the many macro-solar calculators, this design tool models detailed behavior of milliwatt systems in the worst conditions, rather than typical behavior of kilowatt systems in the best conditions. Our simulation suite is validated with a concrete design of micro-solar power systems, the HydroWatch node. With our simulation suite, micro-solar power systems can be designed in a systematic fashion. Putting the model and empirical vehicle together, the design choices in each component of a micro-solar power system are studied to reach a deployable candidate. The deployment is evaluated by analyzing the effects of different solar profiles across the network. The analysis from the deployment can be used to refine the next system-design iteration.

Categories and Subject Descriptors: C.5.m [**Computer System Implementation**]: Miscellaneous; D.4.7 [**Operating Systems**]: Organization and Design—*Real-time systems and embedded systems*; I.6.4 [**Simulation and Modeling**]: Model Validation and Analysis; I.6.5 [**Simulation and Modeling**]: Model Development—*Modeling methodologies*; I.6.8 [**Simulation and Modeling**]: Types of Simulation—*Discrete event*

General Terms: Algorithms, Design, Experimentation, Measurement, Verification

Additional Key Words and Phrases: Micro-solar power system, modeling, simulation, deployment, validation

ACM Reference Format:
Jeong, J. and Culler, D. 2012. A practical theory of micro-solar power sensor networks. ACM Trans. Sensor Netw. 9, 1, Article 9 (November 2012), 36 pages.
DOI = 10.1145/2379799.2379808 http://doi.acm.org/10.1145/2379799.2379808

1. INTRODUCTION

1.1. Motivation

One of the visions of wireless sensor networks (WSNs) is autonomous long-term monitoring of the environment, and a key limiting factor is the ratio of energy consumption and supply. Most sensornet applications in outdoor environments run on battery, since it is easily accessible in off-the-grid environments and is relatively inexpensive.

A portion of this paper is an amplification of Taneja et al. [2008]. "Design, modeling, and capacity planning for micro-solar power sensor networks" in *Proceedings of the 7th International Conference on Information Processing in Sensor Networks*.

This work was supported by the Defense Advanced Research Projects Agency (grant F33615-01-C-1895), the Keck Foundation (grant HydroWatch Center), the National Science Foundation (grant 0435454 "NeTS-NR", 0454432 "CNS-CRI"). This work was also supported by Korea Foundation for Advanced Studies Fellowship, as well as generous gifts from the Hewlett-Packard Company, Intel Research, and California MICRO.

Authors' addresses: J. Jeong, Cisco Systems, San Jose, CA; email: jajeong@cisco.com; D. Culler, Computer Science Division, UC Berkeley, Berkeley, CA; email: culler@eecs.berkeley.edu.

DOI 10.1145/2379799.2379808 http://doi.acm.org/10.1145/2379799.2379808

However, a battery-powered application is not suitable for a long-term deployment due to the finite capacity of the energy storage and the battery capacity to power-consumption ratio. In order to address the limited-lifetime problem, many solutions have been proposed at the application level [Madden et al. 2002; Nath et al. 2004; Pradhan et al. 2002] and networking level [Polastre et al. 2004; Ye et al. 2004, 2006]. These solutions lengthen the lifetime of a sensor network by using various techniques to reduce power consumption, such as aggregation, data compression, and radio duty cycling, though the improvement is only a constant factor and does not solve the limited-lifetime problem. Renewable energy sources, such as solar radiation, vibration, human power, and air flow could be used to solve this problem, as a renewable energy-powered node can potentially run for a long period of time without requiring the replacement of the battery. Among these renewable energy sources, solar energy is the most promising for an outdoor wireless sensornet application. It has higher power density than other renewable energy sources, and this allows a sensor node to collect sufficient energy with a small form factor. Also, it is available for several hours per day in most outdoor locations, whereas the availability of other renewable energy sources is very localized.

Recognizing the possibility of long-term autonomous operation, several implementations have been made [Zhang et al. 2004; Jiang et al. 2005; Raghunathan et al. 2005; Simjee and Chou 2006; Park and Chou 2006]. These implementations demonstrate that building a sensornet system with solar energy harvesting is possible. However, they address only particular points in the design space of micro-solar power systems, rather than providing a general model. These implementations do not provide guidance when they are placed in a setting different from their target environment, or if a different configuration of micro-solar power system is used. In order to explore possible choices in the design space of micro-solar power systems, a general model is needed. A number of previous models have been made [Kansal et al. 2007; Moser et al. 2006b; Sober et al. 2007; Shnayder et al. 2004; Park et al. 2001; Dave et al. 1975; Varshney et al. 2007], but they have focused only on a particular component and not on the whole system.

The goal of this article is to enable the systematic design of a micro-solar power system so that it will be possible to model and analyze hypothetical designs. We first provide a theory of micro-solar power systems, then, based on the theory, we develop simulation tools that reflect reality. The simulation tools enable us to predict the behavior of hypothetical designs and thus deploy only the working ones. Our simulation tools estimate the electrical behavior of micro-solar power systems in a similar way to those of Spice [Newton 1978], the de facto standard circuit simulation tool. However, the time scales are different, for while Spice is usually used for modeling the short-term behavior of a circuit (microseconds to seconds), our simulation tools model the system behavior for a long period of time, such as months and years.

While our simulation tools are made for micro-solar power systems (small low-power electronics with a solar panel measured in milliwatts of power), many tools and calculators are available for *macro-solar* and *meso-solar* installations in residential and commercial applications on the scale of kilowatts. Macro-solar and meso-solar systems have the same basic component categories and the same interconnection as a micro-solar power system, but they differ greatly in the sizes and relative sizes of these components, which lead to very different design and deployment issues. One difference is that with a micro-solar power system, the load is on the same scale as the management, and the system as a whole has to be very efficient and well matched. Another difference is that a micro-solar power system should be planned for the environment that it must deploy in, such as a deep dark forest, rather than the environment that is desired, such as a well-exposed rooftop.

1.2. Problem Statement

Solar energy is considered a viable solution for powering outdoor wireless sensor network applications due to its high power density and wide availability. However, it has a few challenges that make the direct implementation of a micro-solar power system difficult: (i) large design space, (ii) long time scale, (iii) different environments for development and deployment sites, (iv) variability of solar energy.

Typically, a micro-solar power system consists of several components which collect the solar energy, buffer the energy in the energy storage, or consume the energy for computation and communication. Given that there are n-different ways of building each component, the complexity of building a whole system increases as a polynomial in n—building and testing all these combinations is not a practical solution. Further, the problem of the large design space is exacerbated by the long time scale of development and deployment, as developing the hardware and measuring the solar energy profile for verification of a design point may take months. One mistake in the development and deployment cycle requires repeating the entire cycle and delaying the actual deployment. The classic argument for a simulator works here: we can find a suitable design of micro-solar power systems by running simulations without having to implement all the possible designs. We can also keep the development and deployment cycle short with simulation by choosing only the designs that pass simulation tests and then eliminating all others.

A micro-solar power system is usually developed in an indoor environment, but it is deployed in an outdoor location whose solar energy profile varies greatly from one location to another. Thus, the development of a micro-solar power system requires modeling the solar energy profile for the deployment site. However, it is not easy to give a prediction of the solar energy in a straightforward way, because solar radiation depends not only on astronomical factors (e.g., time and location) but also on local effects (e.g., weather and obstructions).

Our simulation tools can predict the variability of solar energy due to astronomical factors and can also refine the solar energy estimation using local factors when they are available. We have designed and implemented a reference hardware platform and a simulation tool suite for micro-solar power systems. The deployment results show that the estimate from our simulation tools is very close to the measurement in reasonably clear weather. This implies that our simulation tools can predict the solar profile well, even in the presence of obstructions. On cloudy or rainy days, the estimation error increases, but it was bounded to about 30%. This implies that it is possible to design a micro-solar power system for long-term survival under varying weather conditions by having a modest surplus in the solar collector.

Our simulation tools are based on a practical theory of micro-solar power systems which consists of two parts: (i) description of the characteristics of each component and their relations, and (ii) event-driven temporal modeling of the interconnected whole. It is a common wisdom in computer science that a large, complex system can be described easily by smaller, more manageable components and their relations. This *divide and conquer* concept also applies to micro-solar power systems, so as a natural approach, we divide a micro-solar power system into multiple functional units whose characteristics are well defined. These components are the external environment, solar collector, input regulator, energy storage, output regulator, and load. We model the relations of these six components in terms of energy flow, operating range, and efficiency, and have verified these based on the measurements of the reference platform. The second part of the theory builds a formal simulation model based on these relations and the descriptions of each component. Using this framework, we have built a formal model for several components using analytical or empirical methods depending on how well its characteristics are defined. Our simulation tools are similar to Spice in that both

estimate the electrical behavior of a system using a discrete time simulator, but they differ in which time scales are used. While Spice is usually used for modeling the short-term behavior of a circuit (microseconds to seconds), our simulation tools model the system behavior for the long-term, such as months and years. Our simulation tools are configured with a coarse-grained time scale that is optimized for fast evaluation and long-term prediction without losing the accuracy within a diurnal behavior.

1.3. Contributions

The contributions of this article are as follows. (i) We provide an architecture of micro-solar power systems; (ii) we build a formal simulation model for micro-solar power systems; (iii) and we develop a reference platform and provide a realistic validation of the simulation model based on it.

1.4. Roadmap

This article is organized into six sections. Section 2 compares outdoor solar energy with other types of energy sources and identifies it as a feasible solution for powering outdoor wireless sensor network applications. It then provides a background overview of solar energy harvesting in the domain of wireless sensor networks. Section 3 presents an architecture of micro-solar power systems, describing the characteristics of its key components and the relationships among its components. Section 4 develops the architecture of micro-solar power systems into a formal simulation model: first, by formalizing each component, then, by synthesizing different variations of models and validating the simulation model with benchtop experimental results. Section 5 describes a reference platform for micro-solar power systems, the HydroWatch node; then, it develops a simulation model of the reference platform and validates the model using deployment data from urban and forest watershed environments. Finally, Section 6 concludes this article.

2. BACKGROUND

2.1. Wireless Sensor Networks and Energy Sources

In general, a wireless sensor node is composed of a micro-controller, communication subsystem, sensor/actuator subsystem, storage subsystem, and power subsystem. In this article, we focus on the design space of the power subsystems, viewing the rest of the system as the load. Depending on the characteristic of the energy source, the power subsystem of a wireless sensor node can be categorized into three types: (a) non-rechargeable battery-powered, (b) wire-powered, and (c) renewable energy-powered.

Using a non-rechargeable battery [Szewczyk et al. 2004; Kim 2007] is the most common way of supplying energy to a sensor node because it is relatively inexpensive and the sensor node can be placed anywhere without requiring the existing power infrastructure to be re-wired. However, it can be problematic in that the lifetime of the sensor nodes is limited due to its limited capacity, as illustrated in Figure 1. In a wireless sensor network testbed, a wired backchannel is used for maintenance purposes, such as reprogramming and data downloading. As a side effect of using a wired backchannel, the sensor node can be powered through the wire [Werner-Allen et al. 2005; Polastre et al. 2005; Handziski et al. 2006]. While wire power makes it easy to maintain a testbed, it is limited to where wiring is available. In an outdoor deployment, wire power may not be available, and making such devices weather proof or wildlife safe can add huge cost and complexity.

A renewable energy-powered node runs on a renewable energy source, such as solar radiation, vibrations, human power, or air flow, and is expected to run for a long period of time without requiring the replacement of the battery. Among the various renewable

Great Duck Island [Szewczyk 04] (Low Duty-Cycle App)	
Sampling Rate	**8.33 x 10-4 Hz**
TX Rate	**0.03 B/s**
Power Consumption	**1.6 mW**
Battery Capacity	**860mAh**
Lifetime	**63 days**

Golden Gate Bridge [Kim 07] (High Sampling Rate App)	
Sampling Rate	**1 KHz**
TX Rate	**441 B/s**
Power Consumption	**358.2 mW – 672.3 mW**
Battery Capacity	**4 x 18000mAh at 6V**
Lifetime	**35 days**

Fig. 1. Examples of sensornet applications that run on non-rechargeable batteries.

Table I. Power and Power Density of Renewable Energy Sources

Energy Source	Power	Power Density
Outdoor Solar [Sikka et al. 2006]	135.6 mW (daily average)	1390 uW/cm^2
Indoor Solar [Roundy et al. 2003]	2.9 mW (20 cm under lamp) 42 uW (ambient office light)	366 uW/cm^2 5.30 uW/cm^2
Vibrations [Roundy 2003]	180 uW	180 uW/cm^3
Human Power [Paradiso 2006]	10 mW	148 uW/cm^2
Wind [Park and Chou 2006]	47.25 mW (wind speed 8.3 m/s)	

energy sources, we focus on outdoor solar energy in this article for two reasons. First, outdoor solar energy has higher power density than other renewable energy sources, and this allows us to build a solar energy harvesting system with a small form factor (Table I). Second, the commercial availability of solar panels allows us to focus on the energy harvesting system from the perspective of computer science, which consists of synthesis, modeling, and analysis, without the need to build the energy harvesting material itself. Note that the preceding statement is made for small-scale outdoor sensor network systems. For a large-scale system, wind energy is preferred over solar energy for scalability, as a wind generator can be made in large scale more easily and cost effectively than a solar power system that requires patches of multiple solar panels and controllers. For an indoor system, solar energy is not so effective due to very low power density, whereas vibrations can be a good source of energy where continuous vibrations occur.

2.2. Prior Work on Micro-solar Power Systems

2.2.1. Micro-Solar Power System Platforms. First, we can categorize micro-solar power systems depending on the type of energy storage and its charging management. The NiMH battery is one of the most popular types of energy storage for micro-solar power systems, because it has relatively high energy density and its charging method is simple (trickle charging) [Raghunathan et al. 2005; Corke et al. 2007; Taneja et al. 2008]. The Li-ion or Li-polymer battery has the highest energy density and a high charge-to-discharge efficiency. This makes the Li-ion battery a good candidate for energy storage when the micro-solar power system needs a small form factor [Zhang et al. 2004; Jiang et al. 2005; Dutta et al. 2006]. However, the charging mechanism of a Li-ion battery is more complicated, because it requires a dedicated charging management chip or software control to correctly control the battery. A *supercapacitor* is a capacitor whose capacity is high enough to be used as energy storage for low-power electronic devices. While its capacity is still much smaller than other types of batteries, its very high maximum recharge cycles allows it to be used for long-lifetime applications [Simjee and Chou 2006]. Some micro-solar power systems used multiple levels of storage that consist of a supercapacitor and a Li-ion battery [Jiang et al. 2005; Dutta et al. 2006; Park and Chou 2006] or a NiMH battery and a Li-ion battery [Ingelrest et al. 2010]. The charging management is more complicated for a hybrid storage system, because it has to choose which storage to charge and when to charge. While the charging controller

can be made in hardware, it can also be made in software by using the sensing and actuation capability of a sensor node.

Since the output power of a solar panel bounds the available energy for a micro-solar power system, a well-designed system should keep the operating point of the solar panel closely to the maximum power point so that the maximum output of power can be transferred from the solar panel. The operating point of the solar panel is determined by either an input regulator or energy storage, depending on whether an input regulator is present. We can categorize published designs of micro-solar power systems depending on how the operating point of the solar panel is determined. First, most NiMH battery-based designs have the solar panel operating point set to the voltage level of the energy storage [Raghunathan et al. 2005; Corke et al. 2007; Taneja et al. 2008]. These designs use the fact that the voltage range of the NiMH, while charging, is relatively narrow. They can achieve near-optimal performance by choosing the solar panel that has its maximum power point in the charging range of the NiMH battery. Second, the operating point of the solar panel can be set to a fixed range [Zhang et al. 2004]. Third, maximum power point tracking should be used for a supercapacitor-based system [Simjee and Chou 2006; Park and Chou 2006]. This is because the supercapacitor has a wide operating range, and its energy transfer is not efficient when the operating point of the supercapacitor is far from the maximum power point of the solar panel.

2.2.2. Micro-Solar Power System Models. As for models for micro-solar power systems, some of the previous research has shown that duty cycle [Jiang et al. 2005; Kansal et al. 2004, 2007; Vigorito et al. 2007; Ingelrest et al. 2010], task scheduling [Moser et al. 2006a], or energy harvesting-aware programming language [Sober et al. 2007] could be adjusted dynamically, depending on the environment, in order to achieve higher utilization and meet the scheduling deadlines. For estimating power consumption of sensor nodes, simulators [Shnayder et al. 2004; Park et al. 2001; Simon et al. 2003; Sundresh et al. 2004; Landsiedel et al. 2005] or trackers [Dunkels et al. 2007; Fonseca et al. 2008] can be used. They estimate power consumption by correlating power consumption events in simulation or actual execution with the pre-recorded energy consumption profile of the target sensor node platform. Estimation of the battery capacity or lifetime is necessary to accurately estimate the behavior of a micro-solar power system. While modeling the battery behavior as a stand-alone device is a well-established topic [Rao et al. 2003; Pop et al. 2005], several simulators are proposed for estimating the battery behavior in a system for wireless sensor networks [Park et al. 2000; 2001; Varshney et al. 2007].

As a way of estimating solar radiation, an astronomical model or a meteorological database can be used. With an astronomical model, we estimate the solar radiation using parameters that affect the angle between the sunlight and the solar panel. When the angle of sunlight from the normal to the solar panel is given, the effective sunlight that shines on the solar panel is proportional to the cosine of the angle [Dave et al. 1975]. Meteonorm[1] is a meteorological database covering over 30 years of solar radiation measurements from a number of locations around the world. In case a location is not in the database, Meteonorm estimates its approximate solar radiation based on its geographic characteristics and matches it to the data of previously known locations. A hybrid model, which refines an astronomical model with a meteorological database, can be used to take advantages of the two approaches: generality and higher accuracy. One example of a hybrid model is the Digital Elevation Model [Dubayah and Rich 1995; Tovar-Pescador et al. 2006; Ingelrest et al. 2010]. The Digital Elevation Model takes topographic information around the site, such as altitude and distance, to calculate

[1]`http://www.meteotest.ch/pdf/am/mn_description.pdf`.

the minimum angle the sunlight can directly reach for every direction. This minimum angle, which is called the *artificial horizon*, is used to account for reduction of solar radiation due to natural obstacles, such as hills. Validating a solar radiation model typically requires some amount of deployment effort to take measurements of a real system on various conditions and compare them with the model. This effort can be alleviated by a solar panel emulator [Li and Chou 2004] that emulates the behavior of the solar panel for a given profile.

2.2.3. Relation to Macro-Solar Power Systems. Macro-solar and meso-solar power systems are commercial and residential solar energy-harvesting installations and use a scale of kilowatts and watts. A micro-solar power system, however, is a small, low-power electronics with a solar panel of less than 1 watt of power. Macro-solar and meso-solar systems have the same basic component categories and the same interconnection as a micro-solar power system. The difference is the relative sizes, which translates into differences in the design and deployment of a micro-solar power system. First, with a micro-solar power system, the load is on the same scale as the management of the system, and the system as a whole has to be very efficient and well matched. Second, with a micro-solar power system, the device is located where the measurement must be taken, not where the sun is best. Thus, a micro-solar power system should be planned for the environment that exists, rather than be planned for the environment that is desired. There are many calculators for macro-solar power systems (National Renewable Energy Laboratory[2]; Iowa Energy Center[3]; California Solar Initiative[4]; Weather Underground[5]). Concepts from these tools can be applied to micro-solar power systems, but they are not suitable for modeling the dynamics of a micro-solar power system. First, they model only the average or maximum performance and cannot predict the varying performance with different operating points. Second, due to economic reasons, they assume that energy surpluses are sold to the grid, whereas micro-solar power systems accumulate the energy surpluses into the energy storage because they are often placed where grid power is not available.

3. ARCHITECTURE OF MICRO-SOLAR POWER SYSTEMS

In general, any solar-powered system consists of the following six components: external environment, solar panel, input regulator, energy storage, output regulator, and load (Figure 2). The solar energy from the environment is collected by the solar collector and is made available for the operation of the load. The energy storage is used to buffer the varying energy income and distribute it to the load throughout the duration. The input regulator can be used to adjust the mismatch between the operating range of the solar panel and the energy storage, while the output regulator is used to shape the operating range of the energy storage to that of the load. The design decisions for each component will dictate the energy flow between them and the overall behavior of the system. In the rest of this section, we describe the architecture of a micro-solar power system in terms of the energy flow of each component.

3.1. External Environment

The amount of solar radiation $P_{solar\text{-}in}$ depends on the environment and places an upper bound on the maximum energy output of the solar collector P_{sol}. In this article, we describe three ways to estimate solar radiation: (a) an astronomical method, (b) an

[2]PVWATTS: A Performance Calculator for Grid-Connected PV Systems. `http://rredc.nrel.gov/solar/codes_algs/PVWATTS`.

[3]Solar Data for Iowa Locations. `http://www.energy.iastate.edu/renewable/solar/calculator`.

[4]Incentive Calculator. `http://www.csi-epbb.com`.

[5]Solar Calculator. `http://www.underground.com/calculator/solar.html`.

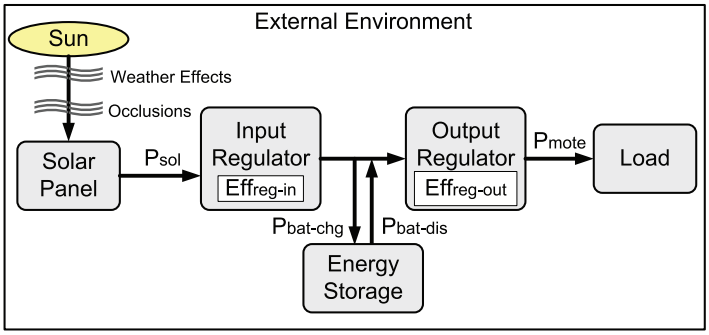

Metric	Description
$P_{solar-in}$	Total incident solar radiation.
P_{sol}	Power produced by the solar panel.
$P_{storage-in}$	Power collected by the solar-collector.
$P_{bat-chg}$	Power stored in the energy storage.
$P_{bat-dis}$	Power extracted from the energy storage.
P_{mote}	Energy consumed by the mote.
Eff_{reg-in}	Efficiency of the input regulator.
$\text{Eff}_{reg-out}$	Efficiency of the output regulator.

Fig. 2. Model for a solar-powered sensor system.

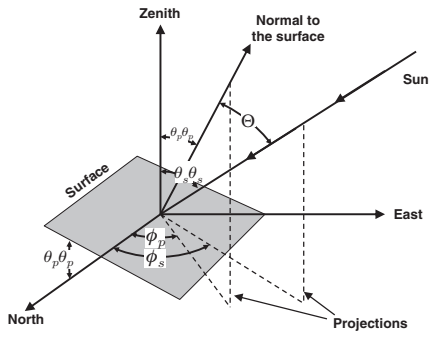

Parameters for astronomical method	
Θ	: Angle of sunlight from normal to the solar panel ($0^\circ \le \Theta_p \le 180^\circ$)
t	: Hour of the day ($0 \le t \le 24$)
n	: Day of the year ($0 \le n \le 365$)
L	: Latitude ($-90^\circ \le L \le 90^\circ$)
θ_p	: Panel inclination ($0^\circ \le \theta_p \le 180^\circ$)
ϕ_p	: Panel orientation from north ($0^\circ \le \phi_p \le 360^\circ$)
θ_s	: Angle of sunlight from its projection to the local vertical ($0^\circ \le \theta_s \le 180^\circ$)
ϕ_s	: Angle of sunlight from its projection to the local true north ($0^\circ \le \phi_s \le 360^\circ$)
δ	: Declination of the sun
$\cos\Theta = \cos\theta_p \cdot \cos\theta_s + \sin\theta_p \cdot \sin\theta_s \cdot \cos(\phi_p - \phi_s)$	
$\cos\theta_s = \sin\delta \cdot \sin L + \cos\delta \cdot \cos L \cdot \cos h$	
$\sin\phi_s = -\cos\delta \cdot \sin h . \sin\theta_s$	
$x = 2\pi n . 365$	
$h = 15(t - 12)$	
$\delta = 0.302 - 22.93\cos x - 0.229\cos 2x - 0.243\cos 3x + 3.851\sin x + 0.002\sin 2x - 0.055\sin 3x$	

Fig. 3. Definition of the angles used in the astronomical method (courtesy of Dave et al. [1975]).

astronomical method with history of weather effects, (c) an astronomical method with local enhancements.

With an *astronomical model*, we estimate the solar radiation using the parameters that affect the angle between the sunlight and the solar panel. According to Dave et al. [1975] (Figure 3), the effective sunlight that shines on the solar panel is proportional to $\cos\Theta$, when the angle of sunlight from the normal to the solar panel is Θ ($0^\circ \le \Theta \le 180^\circ$). Depending on whether the sunlight is above or below the horizon, the solar radiation rate is given as $\cos\Theta$ (when $0^\circ \le \Theta \le 90^\circ$), or 0 (when $90^\circ \le \Theta \le 180^\circ$). Thus, the solar radiation rate can be represented as $\max(\cos\Theta, 0)$. The solar radiation rate $\max(\cos\Theta, 0)$ is a function of several parameters: solar panel inclination θ_p, panel orientation ϕ_p, latitude L, time of the day t, and day of the year n. With an

astronomical method with history of weather effects, we estimate the solar radiation under the influence of weather effects by using the history of solar radiation measurements. In order to get such a history, we can use a meteorological database software suite such as Meteonorm[1], which estimates solar energy radiation as a monthly solar radiation E_{month} (kWh/m^2). Using E_{month}, we can calculate the peak solar hours (PSH), which is the equivalent number of solar radiation hours per day, assuming that the same amount of solar energy is given at a uniform intensity of $1kW/m^2$. Then, the available energy from a specific solar panel for one day, $E_{sol\text{-}day}$, can be estimated as the product of the PSH and the solar panel output power P_{panel} at $1kW/m^2$ (usually provided by its manufacturer).

$$E_{sol\text{-}day} = \text{PSH} \cdot P_{panel} = \frac{E_{month} \cdot P_{panel}}{1kW/m^2 \cdot \#\text{days}}.$$

As well as weather effects, occlusions from local objects, such as trees and buildings, can affect solar radiation. With an *astronomical method with local enhancements*, we refine the solar radiation estimate from the astronomical method with a measurement of local obstructions. An astronomical model with local enhancements is similar to the Digital Elevation Model [Dubayah and Rich 1995; Tovar-Pescador et al. 2006; Ingelrest et al. 2010] in that it refines an astronomical model with previous measurements but uses a different method to estimate local obstructions. It uses samples of solar radiation measurements from a micro-solar node itself instead of topographic information, and this allows it to estimate solar radiation under local obstructions more accurately, because typical topographic information from aerial photographs and satellite images is available in a coarse grain and does not capture obstructions due to smaller objects.

3.2. Solar Collector

A *solar panel* transforms available incident solar radiation to electrical power. A given panel is characterized by its I–V curve (Figure 4) and, in particular, three points: the open-circuit voltage (V_{oc}), short-circuit current (I_{sc}), and maximum power point (MPP). Internally, these are determined by the serial and parallel composition of the solar cells and the total area of the panel. Increasing temperature depresses the I–V curve somewhat, reducing the power output. For the large, expensive panels used in macro-solar installations, these factors are accurately characterized in datasheets and well validated. For the small, inexpensive panels used in micro-solar applications, empirical characterization is often required. More importantly, the operating point of the I–V curve is determined by the load experienced at the panel, which is determined by the input regulator, storage facility, and downstream load. For most panels, the I–V curve is nearly flat for voltages less than that of the MPP, so power increases nearly linearly with the voltage in this range. The operation of a solar panel under a specific radiation condition can be modeled by the I–V curve of the solar panel and the solar radiation rate $RR(t)$ ($0 \le RR(t) \le 1$).

$$I_{panel} = \text{IVCurve}(V_{panel}), \tag{1}$$

$$I_{rad}(t) = RR(t) \cdot I_{panel}, \tag{2}$$

where I_{panel} and V_{panel} are the current and the voltage of the solar panel, and I_{rad} is the current of the solar panel at a given radiation condition. In the preceding formula, we used the solar radiation rate $RR(t)$ to adjust the actual solar panel current for the time-varying solar radiation.

For a long-term estimation, we need to introduce additional adjustment factor R_d to consider the case in which the solar panel gets dirty over time and the actual solar panel current deteriorates.

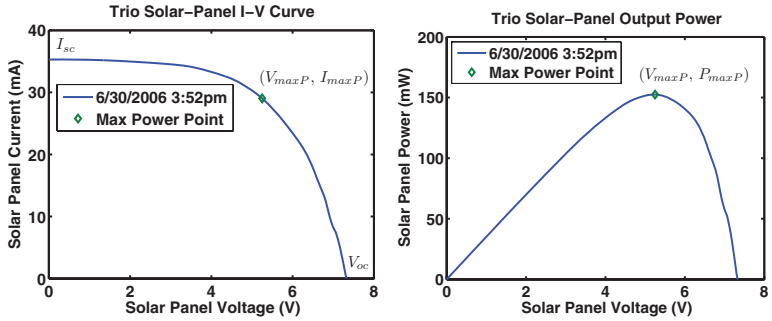

(a) I–V curve. (b) P–V curve with MPP.

Fig. 4. Characteristics of a solar panel.

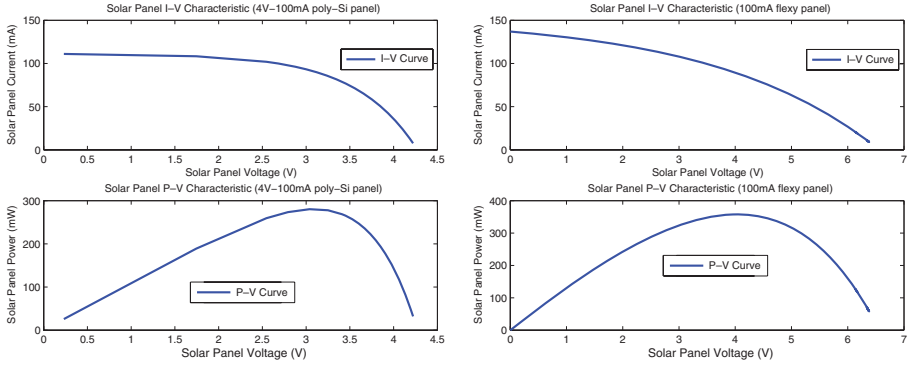

(a) poly-Si panel. (b) Fexible thin film panel.

Fig. 5. Characteristics of a solar panel.

The shape of an I–V curve is determined by the fill factor, the ratio of power at the maximum power point, and the product of the open-circuit voltage and short-circuit current, $FF = P_m/(V_{oc} \cdot I_{sc})$, $0 < FF < 1$. Fill factor can be used as a measure of efficiency for a solar panel—a solar panel gets higher current at a given voltage, thus higher power, as the fill factor becomes closer to 1. Fill factor is a property of each type of solar panel, and it becomes smaller as series resistance increases [Castaner and Silvestre 2002]: $FF = FF_0 \cdot (1 - R_s \cdot I_{sc}/V_{oc})$, where FF_0 is the fill factor for zero series resistance and R_s is series resistance, that is, the resistance serial to an ideal model of solar cell that consists of a current source and a diode. Figure 5 shows I–V and P–V curve for two different types of solar panels: poly-Si panels and flexible thin film panels. We can see that the poly-Si panel has a higher fill factor.

3.3. Input-Power Conditioning

The *input regulator* conditions the output of the panel to meet the operational constraints of the particular battery, including voltage limits, current limits, and charge duration. The operation of an input regulator can be modeled by its power efficiency and a transfer function. The power delivered out of an input regulator is proportional to the power from the solar panel and the power efficiency of the input regulator. The input regulator sets the operating point of the solar panel, interconnecting with the energy storage. Depending on the type of input regulator being used (e.g., no-input

regulator or constant-input-voltage regulator), the voltage of the solar panel V_{panel} can follow the voltage of the energy storage V_{stor} or can be set to a constant.

$$P_{in-reg} = \text{Eff}_{in-reg} \cdot P_{panel}, \tag{3}$$

$$V_{panel} = (V_{stor} + V_{th-schottky}) \text{ or } const, \tag{4}$$

where P_{panel} is the voltage of the solar panel, P_{in-reg} is the voltage of the input regulator, and $V_{th-schottky}$ is the threshold voltage of a diode between the solar panel and the input regulator. In a micro-solar power system, an input regulator can be used to set the specific operating point of the solar panel to meet the operational constraints of the particular energy storage using voltage limits, current limits, and charge duration. While matching the operating points of the solar panel and the energy storage is an advantage of using an input regulator, the sub-unity efficiency of the input regulator is a drawback. The efficiency of an input regulator, Eff_{reg-in}, is 50% to 90%, depending on the part being used. Thus, the analysis of the possible gain of the operating point matching against the inefficiency of the input regulator should be made before it is used in a micro-solar power system.

3.4. Energy Storage

As for *energy storage*, a wide range of battery configurations and chemistries are available for storing charge, as well as supercapacitors—all with differing operating voltages, charge algorithms, and complexities. From a system design perspective, it is desirable for the power subsystem to be able to charge a fully discharged battery without software in the loop so that when placed in sunlight, the device is guaranteed to eventually become active. The portion of energy transferred into the battery during the day and discharged during the night incurs an additional round-trip transfer efficiency, Eff_{stor}, about 66%[6] for NiMH chemistries. The capacity of the battery determines not only the potential lifetime in darkness, but also how much energy can be harvested while the sun shines. In modeling the capacity of the energy storage, the self-discharge rate should be considered, as well as the nominal capacity of the energy storage. The self-discharge rate is determined by storage chemistry and temperature. The energy storage can be modeled by its voltage level, energy level, charge-discharge efficiency, and the voltage-to-energy relationship. The voltage-to-energy relation, V-to-E( ), can be described either analytically or empirically, depending on the type of energy storage. Additionally, the energy-to-voltage relation, E-to-V( ), is its inverse.

$$V_{stor} = \text{E-to-V}(\text{E}_{stor}) \Leftrightarrow \text{E}_{stor} = \text{V-to-E}(V_{stor}), \tag{5}$$

$$\text{E}_{discharged} = \text{Eff}_{stor} \cdot \text{E}_{charged}, \tag{6}$$

where E_{stor} is the stored energy, $E_{charged}$ is the energy being charged, and $E_{discharged}$ is the energy being discharged. For a more accurate model of the capacity for energy storage, the self-discharge rate should also be considered, as well as the nominal capacity. Self-discharge rates vary depending on storage chemistry and temperature.

3.5. Output Power Conditioning

The *output regulator* matches the battery characteristics to the requirements of the mote and protects the battery from low discharge. It, too, is characterized by its efficiency, $\text{Eff}_{reg-out}$, and in particular, its efficiency at two very different operating points: 10s of microwatts most of the time and 10s of milliwatts during short active periods. For a typical bimodal P_{mote}, an effective efficiency of 50% or less is expected. This determines the load experienced by the supply and storage components of the power

[6]With charging rate 0.1C/hour, where C is the capacity of the battery.

Table II. Average Current at Different Duty-Cycle Rates

Duty-cycle rate	1.56%	6.25%	12.5%	25%	50%
I_{est} (mA)	0.54	1.34	2.41	4.54	8.81

Note: I_{sleep} = 0.27mA and I_{awake} = 17.4mA.

subsystem. The operation of an output regulator can be modeled by power efficiency and output voltage. The power delivered out of an output regulator $P_{out-reg}$ is proportional to the load power consumption P_{load} and the inverse of the power efficiency. The output voltage $V_{out-reg}$ is relatively constant when the battery voltage remains within its operating range $[V_{lb}, V_{ub}]$. It becomes zero when the battery voltage becomes below the operating range, and this protects the battery from low discharge.

$$P_{out-reg} = P_{load}/\mathrm{Eff}_{out-reg}, \tag{7}$$

$$V_{out-reg} = \begin{cases} const & \text{if } V_{lb} \le V_{stor} \le V_{ub}, \\ 0 & \text{if } V_{stor} < V_{lb}. \end{cases} \tag{8}$$

For correct operation, an output regulator should be chosen so that the upper bound of its operating range V_{ub} is higher than the upper bound of the battery voltage.

3.6. Load

The sensor node (mote) is the end consumer of energy in our micro-solar power system. The amount of energy a mote consumes (P_{cons}) determines the capacity planning of a solar-powered sensor node. The operation of the load is described by its *average current* and *operating voltage*. The average current I_{load} is determined by the application, and the operating voltage V_{load} is determined by the voltage of the output regulator.

$$I_{load}: \text{ given by application}, \tag{9}$$

$$V_{load} = V_{out-reg}. \tag{10}$$

The average current I_{est} can be estimated with the following formula if the duty-cycle rate R, the current for the sleep state I_{sleep}, and the current for the active state I_{awake} are known.

$$I_{est} = R \cdot I_{awake} + (1 - R) \cdot I_{sleep}. \tag{11}$$

Table II shows the average current for a Trio node [Dutta et al. 2006] at different duty cycles.

3.7. Overall System Behavior

The overall system behavior can be described by surplus power P_{net}, which is surplus power from the solar radiation after being used for load.

$$P_{net} = P_{in-reg} - P_{out-reg}. \tag{12}$$

Depending on whether the surplus is positive, the system is in either recharge or discharge state. When the surplus is positive ($P_{net} > 0$), the system is in recharge state with the energy of $P_{net} \cdot \Delta t$ being charged. When the surplus is nonpositive ($P_{net} \le 0$), the system is in discharge state with the energy of $(\text{-}P_{net}) \cdot \Delta t$ being discharged. It should be noted that surplus power P_{net} is meaningful within a normal operating range of a system; in a well-designed system, charging stops, and the surplus power becomes shunted without being stored if the energy storage is fully charged.

4. DESIGN OF MICRO-SOLAR POWER SYSTEM SIMULATOR

In this section, we present a Matlab-based micro-solar power system simulator and describe its key ideas. The simulator takes a configuration of a micro-solar power

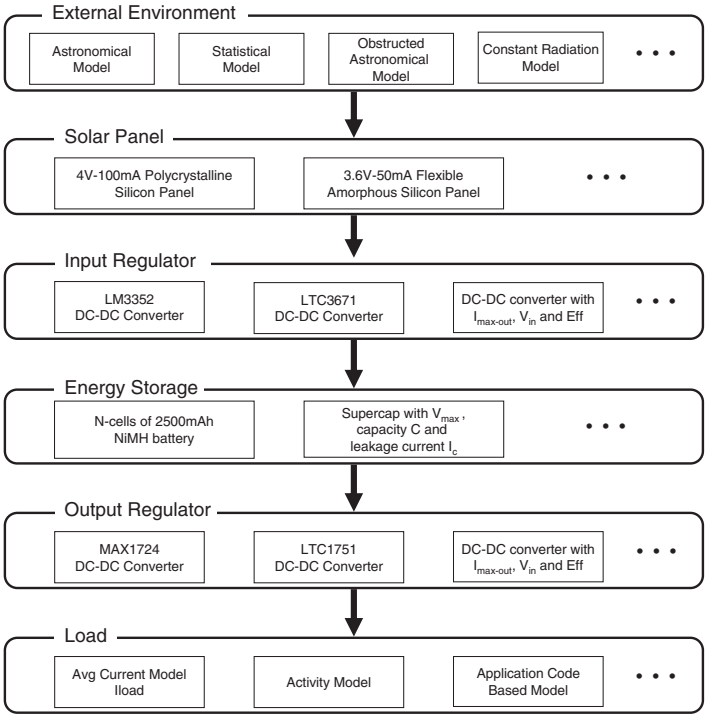

Fig. 6. Modular design of a micro-solar power system simulator.

system along with user-defined data and quickly generates behavior estimates for either a short period or a long period of time.

4.1. Overall Architecture and Principles

The simulator is composed of the following modules: external environment module, solar panel module, input regulator module, energy storage module, output regulator module, and load module. Each module of the simulator describes the behavior of a corresponding component of a micro-solar power system (Figure 6). Our simulator computes the state of each component of a micro-solar power system when the initial condition (e.g., initial battery capacity) and the time-event vector are given. The time-event vector is a tuple of discrete times during the day at which the state of the micro-solar power system will be evaluated. Overall, the estimation accuracy increases as the interval between the evaluation times gets smaller, but, at the same time, the computation time increases in proportion to the inverse of the interval. Once the state of the micro-solar power system is computed for one day, the long-term trend can be computed iteratively. A component of a micro-solar power system has a common generic behavior, but its detailed behavior may vary, depending on what instance of a component is used. Our simulator provides two different ways to customize the behavior of a component: curve fitting and piecewise linear interpolation. The curve fitting method is used when the behavior of a component can be described by a formula or a continuous function. A formula generally consists of a collection of variables, constants and operators. When measurements of the component are available, the curve fitting algorithm determines the unknown constants that minimize the errors between the measured output and the estimated output. Piecewise linear interpolation

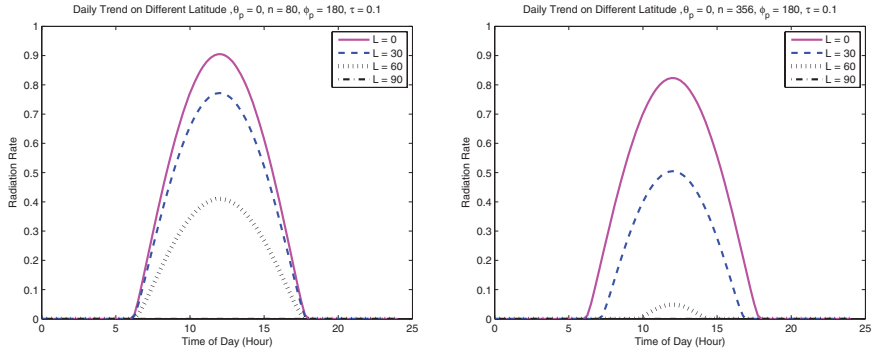

(a) Spring and fall. (b) Winter.

Fig. 7. Astronomical model with effects of latitude and seasonal variation with the solar panel flat ($\theta_p = 0$, $\phi_p = 180$). The day of year n is set to 80 (spring) or 356 (winter), while the latitude L varies.

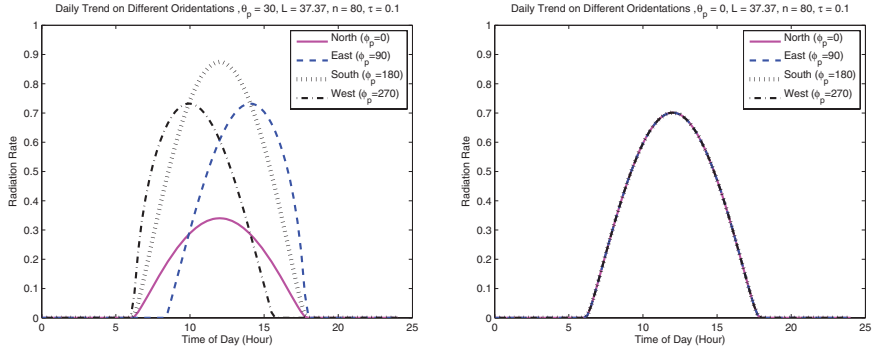

(a) Inclination = 30. (b) Inclination = 0.

Fig. 8. Astronomical model with effects of orientation and inclination on a particular day in mid-March ($n = 80$). The inclination θ_p is set to 30 or 0, while the orientation ϕ_p varies.

is used when the behavior of a component cannot be represented by a single formula. It partitions the input domain so that the behavior of a component is represented as a sequence of piecewise linear functions.

4.2. Modeling Solar Radiation

Our simulator provides a few of ways to model solar radiation: an astronomical model, a statistical model, and an astronomical model with obstruction vector.

4.2.1. Astronomical Model. The astronomical model that was introduced in Section 3.1 estimates the solar radiation rate by calculating the angle Θ ($0^\circ \leq \Theta \leq 180^\circ$) between the sunlight and the normal to the solar panel. We have formulated the astronomical model as a component of our micro-solar power simulator. For example, Figure 7 shows the estimation of the daily solar radiation for different sets of parameters: time of the year n, latitude L, and inclination θ_p, and panel orientation ϕ_p.

4.2.2. Obstructed Astronomical Model. The estimation of solar radiation from the astronomical or statistical model can be a useful tool in understanding the long-term variation of solar radiation, but it deviates from the real measurement in many cases when the solar radiation is obstructed by objects or diffused by weather. In order to improve the accuracy of our simulator on the effects of obstructions, we develop an obstructed

astronomical model using a previously measured obstruction profile. When we estimate solar radiation under obstruction effects, we assume that objects that cause obstructions are stationary, and we can expect the same pattern of obstructions from one day to another. At time t and day n, we can define the following variables.

—$R1(t, n)$. Estimation of solar radiation using an astronomical model.
—$M(t, n)$. Measurement of solar radiation.
—$Ob(t, n)$. Obstruction factor.
—$R2(t, n)$. Estimation of solar radiation using a scaled astronomical model and is given as $S \cdot R1(t, n)$. S is a scaling factor for $R1(t, n)$ so that it can match the envelope of the measurement $M(t, n)$.
—$R3(t, n)$. Estimation of solar radiation using an obstructed astronomical model and is given as $S \cdot R1(t, n) \cdot (1 - Ob(t, n))$.

An obstructed astronomical model requires a reference day n to calculate the reference obstruction profile. When an observation window of k days $W_k = \{n_1, n_2, \cdots, n_k\}$ is given, the reference day n ($\in W_k$) is defined as follows.

$$\forall n_i \in W_k, \sum_{t=t_1}^{t_m} M(t, n) \geq \sum_{t=t_1}^{t_m} M(t, n_i). \tag{13}$$

The reason for observing measurement data over k days is to reduce the effect of weather, such as clouds or rain, and the choice of k can vary depending on location and season. We note that choosing a reference day occurs only once at the beginning of a measurement cycle, not for a whole year. Otherwise, it would defeat the purpose of a prediction model.

Once the reference day n is determined, the scaling factor S can be found. Suppose the measurement of solar radiation $M(t, n)$ has a maximum at time t_{max} over discrete time intervals $[t_1, t_m]$. Then, the scaling factor S is defined as follows.

$$S = \frac{M(t_{max}, n)}{R1(t_{max}, n)}. \tag{14}$$

Using the maximum point $M(t_{max}, n)$ is good for many cases, but it may produce a misleading result, depending on the profile of the solar radiation measurement. In order to remove the case when the maximum point is an outlier within $\alpha\%$, we used a (100-$\alpha/2$)%-percentile point to calculate the scaling factor.

$$S = \frac{M(t_{(100-\alpha/2)\%max}, n)}{R1(t_{(100-\alpha/2)\%max}, n)}. \tag{15}$$

Here, $t_{(100-\alpha/2)\%max}$ is calculated as follows. Suppose $M(t_{min}, n) \leq M(t, n) \leq M(t_{max}, n)$ for $t \in [t_1, t_m]$. Then, $t_{(100-\alpha/2)\%max}$ is the smallest t that meets the following inequality.

$$M(t, n) \geq \frac{100 - \alpha/2}{100} \cdot M(t_{max}, n). \tag{16}$$

For example, $t_{(100-\alpha/2)\%max}$ becomes the median point for $\alpha = 100$ and the 98th percentile point for $\alpha = 4$.

The obstruction factor $Ob(t, n)$ is the relative difference between the scaled astronomical model $R2(t, n)$ and the measurement $M(t, n)$.

$$Ob(t, n) = \begin{cases} \frac{R2(t,n) - M(t,n)}{R2(t,n)} & \text{if } R2(t, n) > 0, \\ 1 & \text{otherwise.} \end{cases} \tag{17}$$

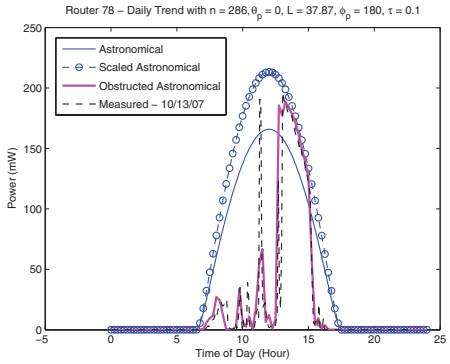

Fig. 9. Estimating the solar radiation using obstruction measurement.

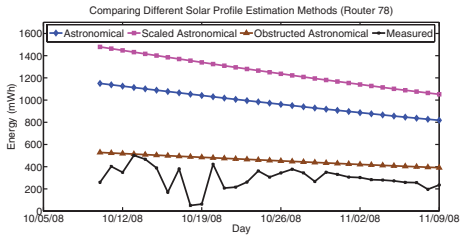

Deviation from the measurement	
Astronomical	68.3%
Scaled astronomical	73.3%
Obstructed astronomical	24.8%

Fig. 10. Daily solar radiation with different estimation methods.

The estimation of solar radiation with the obstructed astronomical model at time t and date n', $R3(t, n')$, is given as $S \cdot R1(t, n') \cdot (1 - Ob(t, n'))$. Since we assume that obstructions are stationary, $Ob(t, n') = Ob(t, n)$. Thus,

$$R3(t, n') = S \cdot R1(t, n') \cdot (1 - Ob(t, n)). \tag{18}$$

While the preceding example used samples from a single day to estimate the scaling factor and the obstruction vector, estimates from multiple days can be used to reduce the error.

Figure 9 shows the measurement $M(t, n)$ with three different solar radiation estimations: the astronomical model $R1(t, n)$, the scaled astronomical model $R2(t, n)$, and the reconstructed astronomical model $R3(t, n)$. A sensor node was placed in a meadow under a tree, and we used the measurement gathered on October 13, 2007, to calculate the scaling factor S and the obstruction factor $Ob(t, n)$. Figure 10 compares the solar radiation of different estimation methods with the measured value. We can see that the reconstructed astronomical model $R3(t, n)$ is very close to the measurement $M(t, n)$ when the weather is sunny. In Figure 10, the estimation error of $R3(t, n)$ is less than 25% on average.

4.3. Modeling Solar Panel

The I–V characteristic of a solar panel can be described with a generic formula [Randall 2005]: $I = I_{sc} - A \cdot (\exp(B \cdot V) - 1)$, where I_{sc} is the short current and A and B are constants. Having a generic formula allows us to determine the I–V characteristic of a solar cell using the curve fitting method. After the I–V characteristic of a solar

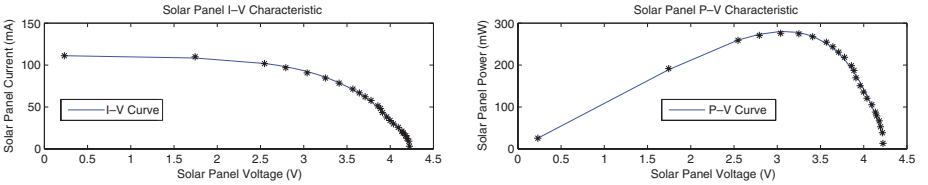

Fig. 11. I–V and P–V graph derived from the measurement of 4V-100mA polycrystalline silicon solar panel with I–V curve fitting constants A = 0.2526 and B = 1.4255.

panel is determined, our model can find the current or power of a solar panel at a given operational voltage. Figure 11 shows I–V characteristics for a 4V-100mA polycrystalline silicon solar panel. The solar panel operates as a voltage-controlled current source. The voltage of the solar panel V_{panel} is determined by the output of the solar panel, which is either a battery or a regulating diode.

$$V_{panel} = \begin{cases} V_{stor} + V_{th-schottky} & \text{with diode,} \\ V_{stor} & \text{otherwise.} \end{cases} \tag{19}$$

Once the voltage of the solar panel is determined, its current and power can be determined by its I–V curve at a given light intensity.

4.4. Modeling Energy Storage

4.4.1. Modeling NiMH Rechargeable Battery. From the perspective of the micro-solar power simulator, NiMH rechargeable batteries have two characteristics: First, NiMH has different characteristics depending on whether it is in charging mode or discharging mode, which makes the problem more complicated. This is because the output voltage of the solar panel depends on the battery voltage, and the battery can be either in charging mode or discharging mode, depending on the solar panel output power. We address this problem by solving the states of all components for a few possible modes and choosing the mode that meets the constraints of the system. Second, while a NiMH rechargeable battery maintains a stable voltage level for a large operating range, its voltage level changes over the stored charge. This capacity-to-voltage characteristic is nonlinear and is not easily represented by a simple formula. In order to represent this characteristic, we use the piecewise linear interpolation method, using the manufacturer-provided datasheet for charging and discharging modes. Figure 12 describes an algorithm that evaluates the system state depending on whether the battery is either in discharge or in charge. The system variables, initial conditions, and functions for this algorithm are listed in the following figure.

4.4.2. Modeling Supercapacitors. For a given voltage level V, the energy level of a supercapacitor E can be calculated using the following formula, and the voltage level can be calculated from the inverse equation: $E = \frac{1}{2}CV^2 \iff V = \sqrt{\frac{2E}{C}}$, where C is the capacitance of the supercapacitor. Our simulator also considers the effect of energy leakage when modeling a supercapacitor, because a supercapacitor has a higher energy leakage rate than a battery, and its effect is noticeable on a large time scale. Using the manufacturer-provided leakage current is one way of modeling the energy leakage of a supercapacitor. When the leakage current is given as I_c and the supercapacitor operates at voltage $V(t)$, the energy leakage $E_{leak}(t)$ at time t for the time duration of Δt can be given by the following formula: $E_{leak}(t) = I_c \cdot V(t) \cdot \Delta t$. Another way of estimating the energy leakage of a supercapacitor is to use an energy-time graph that can be found by measurement or provided by the manufacturer.

1: $C_{next-bat} \leftarrow C_{bat-init}$
2: **for** $i = 1$ to N **do**
3: $C_{bat}[i] \leftarrow C_{next-bat}$
4: $V_{bat-dis}[i] \leftarrow$ **Cap-Vbat-Dis**$(C_{bat}[i])$
5: $V_{bat-chg}[i] \leftarrow$ **Cap-Vbat-Chg**$(C_{bat}[i])$
6: Evaluate system state $S_{dis}[i]$ at discharge using $V_{bat-dis}[i]$.
7: Evaluate system state $S_{chg}[i]$ at charge using $V_{bat-chg}[i]$.
8: Evaluate net battery charging power $P_{net-dis}[i]$ at discharge using $S_{dis}[i]$.
9: Evaluate net battery charging power $P_{net-chg}[i]$ at charge using $S_{chg}[i]$.
10: **if** $P_{net-dis} > 0 \vee P_{net-chg} > 0$ **then**
11: Set system state $S[i]$ as $S_{chg}[i]$.
12: **else**
13: Set system state $S[i]$ as $S_{dis}[i]$.
14: **end if**
15: $C_{next-bat} \leftarrow C_{bat}[i] + (t[i+1] - t[i]) \times P_{net-bat}[i] \triangleleft V_{bat}[i]$
16: **end for**

$t[i]$	Starting time for ith iteration
$C_{next-bat}$	Capacity of battery for next iteration
$C_{bat-init}$	Initial value for capacity of battery
$C_{bat}[i]$	Capacity of battery
$V_{bat-dis}[i]$	Voltage of battery at discharge
$V_{bat-chg}[i]$	Voltage of battery at charge
$S_{dis}[i]$	System state at discharge, which is a collection of variables for each component of the system
$S_{chg}[i]$	System state at charge
$P_{net-dis}[i]$	Net battery charging power at discharge
$P_{net-chg}[i]$	Net battery charging power at charge
$S[i]$	Evaluated system state
$P_{net-bat}[i]$	Evaluated net battery charging power
$V_{bat}[i]$	Evaluated battery voltage
Cap-Vbat-Dis( )	Function that gives voltage at discharge for given capacity
Cap-Vbat-Chg( )	Function that gives voltage at charge for given capacity
Eff	Charge-to-discharge efficiency

Fig. 12. Algorithm that evaluates the state of a micro-solar power system with NiMH battery.

4.4.3. Modeling Other Types of Battery. While we used NiMH battery as an example of battery in Section 4.4.1, other types of battery, such as the Li-ion battery, can also be modeled with our micro-solar power system model in a straightforward way. The system-state evaluation algorithm described in Figure 12 works in the same way. The only changes are the capacity-to-voltage relation parameter (**Cap-Vbat-Dis()** and **Cap-Vbat-Chg()**) and the charge-to-discharge efficiency parameter (**Eff**), which are typically available from the battery datasheet.

4.5. Modeling Output Regulator

The behavior of an output regulator can be described by the following three characteristics: (a) operating range, (b) output voltage, and (c) power efficiency. While these characteristics are provided by the manufacturer, they are mostly nonlinear and have different forms among different parts; thus, we use the piecewise linear interpolation method to model the behavior of an output regulator. Figure 13 shows the estimation of efficiency of a MAX1724 regulator and compares it with manufacturer-provided data.

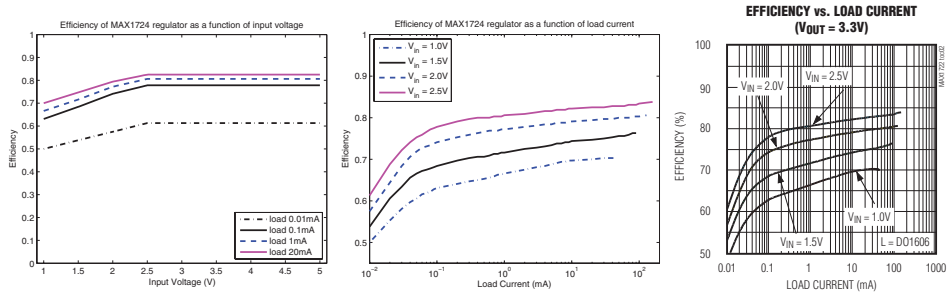

(a) (b) (c)

Fig. 13. Efficiency of the MAX1724 regulator with output voltage 3.3V. (a) Efficiency estimation for varying input voltage; (b) efficiency estimation for varying load current; (c) efficiency from datasheet for varying load current.

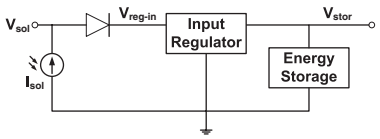

Fig. 14. Configuration of a micro-solar power system with a buck converter as an input regulator.

4.6. Modeling the Input Regulator

Before we model the input regulator, we can consider the behavior of a micro-solar power system with no input regulator. In this case, the solar panel voltage V_{panel} is determined by the voltage level of the energy storage, V_{stor}, and the threshold voltage of the diode, $V_{th-schottky}$, with the following equation.

$$V_{panel} = V_{stor} + V_{th-schottky}. \tag{20}$$

Next, we consider a micro-solar power system with an input regulator; in this system, there is an input regulator between the output of the diode and the input of the energy storage (Figure 14). For easier analysis, we can consider a simple case: a buck converter (step-down DC-DC converter) as an input regulator and a supercapacitor as energy storage. In this system, the buck converter operates in two modes.

(1) Constant-input-voltage mode ($V_{stor} < V_{reg-in-th}$) .
If the output voltage of the input regulator V_{stor} is below a certain level $V_{reg-in-th}$, the buck converter is turned on, and its input voltage locks to the threshold value. The threshold voltage $V_{reg-in-th}$ is a property of a particular type of input regulator. Thus, in constant-input-voltage mode, the solar panel operating point remains constant even though the voltage level of the storage changes due to charge and discharge.

$$V_{reg-in} = V_{th-reg-in} = const, \tag{21}$$

$$V_{panel} = V_{reg-in} + V_{th-schottky} = V_{th-reg-in} + V_{th-schottky} = const, \tag{22}$$

$$I_{panel} = IVCurve(V_{panel}) = const. \tag{23}$$

(2) Pass-through mode ($V_{stor} > V_{reg-in-th}$).
If the output voltage of the input regulator V_{stor} is above the threshold $V_{reg-in-th}$, the buck converter is turned off and looks like a pass-through wire from the outside. In pass-through mode, the solar panel operating point changes along the solar panel IV curve, following the voltage of the storage.

$$V_{reg-in} = V_{stor}, \tag{24}$$

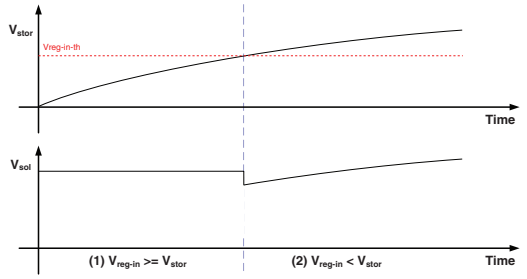

Fig. 15. Operating range of a micro-solar power system with a buck converter as an input regulator.

$$V_{panel} = V_{reg-in} + V_{th-schottky} = V_{stor} + V_{th-schottky}, \tag{25}$$

$$I_{panel} = IVCurve(V_{panel}). \tag{26}$$

Figure 15 shows the case in which a depleted supercapacitor is charged from a solar panel through a buck converter. In the beginning, the voltage level of the supercapacitor V_{stor} is low, meeting the condition for the constant-input-voltage mode; thus, the buck converter is turned on, and its input voltage V_{reg-in} becomes constant due to the characteristic of constant input impedance of the device R_{reg-in}. Then, the solar panel current also becomes constant. As time goes on, the supercapacitor is charged and its voltage level V_{stor} rises. When V_{stor} becomes high enough to meet the condition for the pass-through mode, the buck converter is turned off and the solar panel voltage V_{reg} increases, following the supercapacitor voltage V_{stor}. The solar panel voltage V_{panel} also increases as V_{reg} increases. At the same time, the current of the solar panel I_{panel} decreases along the solar panel IV curve.

4.7. Modeling Load

For modeling the long-term behavior of the load, we can use the average current consumption measured by a scope or a multimeter. This is because most sensornet applications have periodic behaviors of sensing and communication, and any surge in power consumption becomes averaged over a long period of time. In our simulator, we use the average current-based model. For modeling the more dynamic behavior that varies over user input or environment, we can use an application-level power consumption simulator [Shnayder et al. 2004] or a power consumption tracker [Fonseca et al. 2008]. An application-level power consumption simulator correlates the time-simulated power state of each hardware component with the previously taken per-component power consumption table in order to estimate power consumption. This approach does not require any special hardware and can be applied to any sensor platform as long as per-component power consumption is measured. However, it is limited by the availability of an application-level power consumption simulator. A power consumption tracker takes a different approach. It measures the power consumption of a sensor node and logs the power-state changing activity for each hardware component. If this measurement is taken for different values over its parameter space, power consumption at an arbitrary parameter value can be estimated by interpolating previous measurements. While it requires that a sensor node have energy-metering capability, it is advantageous in that its measurement and estimation is based on actual placement not on simulation; thus, it can capture a variation in power consumption due to environment.

4.8. Composition

In this section, we construct a model of the whole micro-solar power system and simulate it based on the description of each component and its interconnection with others.

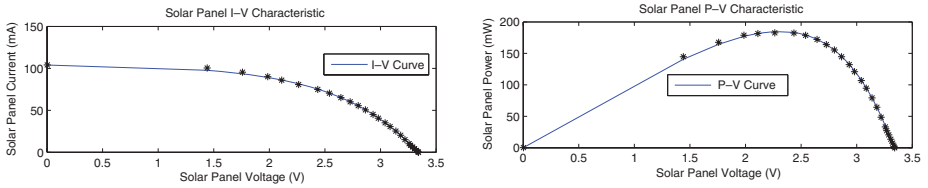

Fig. 16. I–V curve of the 4V-100mA polycrystalline silicon solar panel under the indoor lamp light.

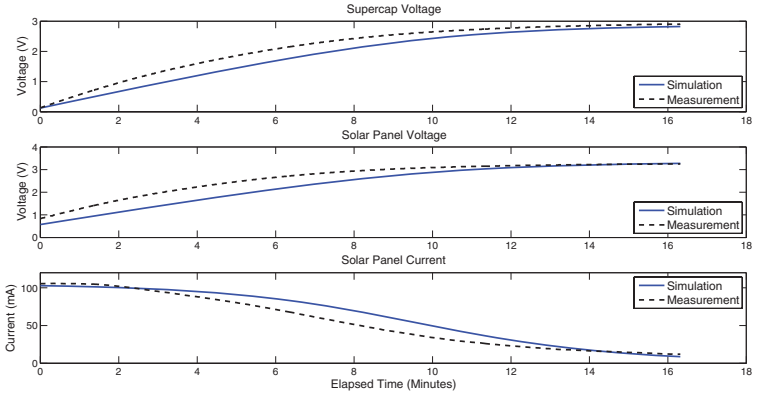

Fig. 17. Trend of solar panel and supercapacitor for a micro-solar power system with 4.0V-100mA solar panel and 22F supercap under the indoor lamp light. No input regulator was used. No load or output regulator was attached. We note that there is a gap between the simulation and the measurement, and this is caused by an idealistic modeling of the Schottky diode. The threshold voltage of the Schottky diode is modeled as a fixed value in our simulator; however, the threshold voltage changes depending on the current in a real system.

We simulate the model of a micro-solar power system in two steps: first, under constant radiation, and second, under the daily solar radiation cycle.

4.8.1. Simulation under Constant Radiation. First, we simulate the effect of an input regulator and verify it with the measurement. The simulation and measurement result with no input regulator, is shown in Figure 17, and we can draw the following observations.

(1) As the supercapacitor is being charged, the solar panel voltage increases, and the solar panel current decreases, because the solar panel voltage follows the supercap voltage, and the solar panel voltage and the solar-panel I–V curve determine the solar panel current. We can see that the simulation captures the effect well.
(2) From empty capacity to near-full capacity, it took about 17 minutes in measurement and 20 minutes in simulation until the supercap was fully charged.
(3) The simulation closely predicts the behavior of the actual system with the correlation coefficient between the simulation result and the measurement 0.9904.

The simulation and measurement result with an LM3671 buck converter as an input regulator is shown in Figure 18, and we can draw the following observations.

(1) As the supercapacitor is being charged, the solar panel voltage and the solar panel current change in two phases: first, the constant-input-voltage mode, and second, the pass-through mode. We can see that the simulation captures this two-phase operation well.
(2) From empty capacity to near-full capacity, it took about 19 minutes in measurement and 20 minutes in simulation until the supercapacitor was fully charged.

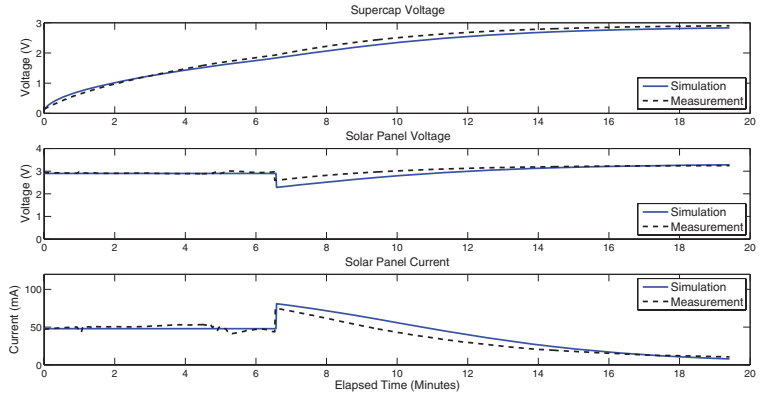

Fig. 18. Trend of solar panel and supercapacitor for a micro-solar power system with 4.0V-100mA solar panel and 22F supercap under the indoor lamp light. LM3671 step-down DC-DC converter was used as an input regulator. No load or output regulator was attached.

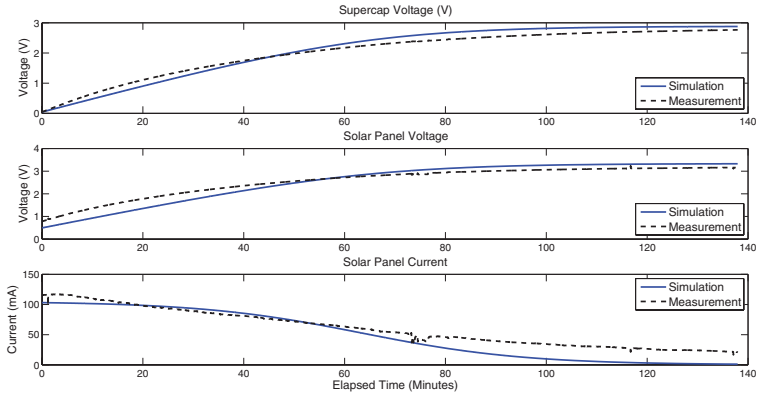

Fig. 19. Trend of solar panel and supercapacitor for a micro-solar power system with 4.0V-100mA solar panel and 140F supercap under the indoor lamp light. No input regulator was used. No load or output regulator was attached. The gap between the simulation and the measurement is caused by an idealistic modeling of the Schottky diode.

(3) The simulation closely predicts the behavior of the actual system with the correlation coefficient 0.9980.

Second, we simulate the effect of different energy storage capacities. For this purpose, we simulate the charging time of supercap-based systems with different energy storage sizes: 22F and 140F. The simulation and measurement results with the 140F supercapacitor (Figure 19) show that the simulation also holds when we increase the energy storage size from 22F to 140F. If we compare this with the charging time of the 22F supercap, we can see that the charging time of a supercapacitor roughly increases in proportion to the capacity of the supercapacitor.

4.8.2. Simulation under Daily Solar Radiation. First, we simulate a micro-solar power system under the average yearly solar radiation (day of year $n = 80$), as shown in Figure 20. As a workload, the HydroWatch[7] workload ($I_{load} = 0.53mA$) was used. The simulation

[7]The HydroWatch node is a micro-solar power system we designed as a reference implementation, and more detail of the HydroWatch node will be discussed later in Section 5.

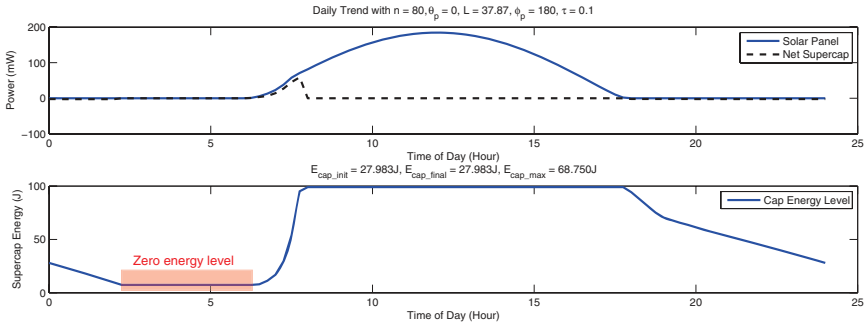

(a) 22F supercapacitor, $I_{load} = 0.53mA$.

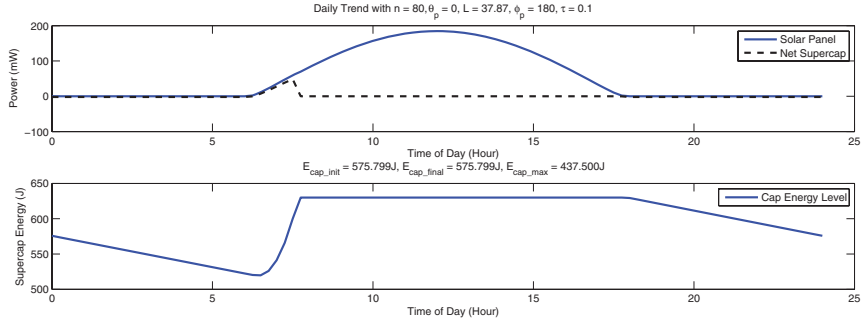

(b) 140F supercapacitor, $I_{load} = 0.53mA$.

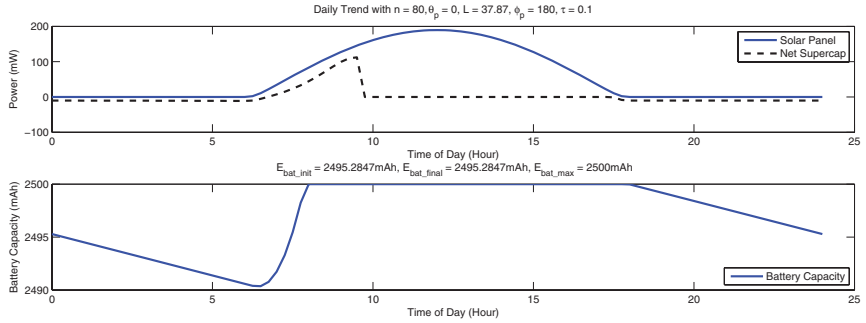

(c) Two 2500mAh NiMH batteries, $I_{load} = 0.53mA$.

Energy Storage	**One 22F supercap**	**One 140F supercap**	**Two 2500mAh NiMH batteries**
Load current I_{load}	0.53 mA	0.53 mA	0.53 mA
Charging time T_c	1 hour 45 minutes	1 hour 30 minutes	1 hour 45 minutes
Discharging time T_d	8 hour 15 minutes	12 hour 15 minutes	12 hour 15 minutes
Discharged energy E_d	91.684J	110.238J	9.636mAh (= 97.130J at 2.8V)

Fig. 20. A micro-solar power system under average yearly solar radiation with HydroWatch workload (day of year $n = 80$). 4.0V-100mA solar panel, MAX1724 step-up DC-DC converter (output regulator), TelosB node (load) and no input regulator was used.

result shows that one 22F supercap cannot provide enough storage for daily operation under average yearly solar radiation, whereas either one 140F supercap or two 2500mAh NiMH batteries can provide enough storage for daily operation. For the last two cases, the charging time T_c, the discharging time T_d, and the discharged energy E_d are about the same, because these two cases have the same load current and radiation condition, which determine the energy consumption and energy supply rate, so the effects of using different energy storage types are not as high.

We notice that the discharging time T_d is limited by the capacity of the energy storage for the case that does not survive an overnight operation (one 22F supercap). For the cases that survive an overnight operation (one 140F supercap and two 2500mAh NiMH batteries), the discharging time T_d is limited by the nighttime extent. We also notice that the discharging time of the first case is about two thirds of the second case (8 hour 15 minutes over 12 hour 15 minutes); this implies that the minimum capacity for a supercapacitor that can survive an overnight operation is about 33F (= 22F * 3/2).

Second, we simulate a micro-solar power system under the worst-case yearly solar radiation (day of year $n = 356$), as shown in Figure 21. With the HydroWatch workload ($I_{load} = 0.53mA$), one 22F supercap cannot provide enough storage for daily operation under average yearly solar radiation, whereas, either one 140F supercap or two 2500mAh NiMH batteries can provide enough storage for daily operation. For these two cases, we notice that the charging time and the discharging time are longer than the case with average yearly solar radiation ($n = 80$), due to the fact that there is a smaller energy budget available during the winter.

5. VALIDATING THE SIMULATOR DESIGN USING A REFERENCE IMPLEMENTATION

In this section, the simulation model of micro-solar power systems developed in the previous section is validated in realistic outdoor experiments using a reference implementation. We first describe the reference implementation of a micro-solar power system, the HydroWatch node. Then, we validate the simulation model using energy flow measurements taken from urban neighborhood and forest watershed deployments.

5.1. Node and Network Design of Reference Implementation

5.1.1. Network Architecture. The sensor node is built around the TelosB-compatible Tmote Sky.[8] The mote software, which provides periodic data acquisition, thresholding, power management, remote command processing, and health monitoring, is a modified Primer Pack/IP.[9] based on TinyOS 2.0. The patch network is an implementation of IPv6 using 6LoWPAN over IEEE 802.15.4 radios [Montenegro et al. 2007]. In the initial HydroWatch deployment at the Angelo Reserve in Northern California (Figure 22), the sensor patch contained 19 nodes over a 220 m x 260 m area stretching across a deep ravine formed by Elder Creek, up the deeply forested north slope of the watershed area, and bending to the east to a particular tall stand of Douglas Fir trees. The transit network between the base station and the patch was implemented using the same node and link technology as the patch, so there is no specific gateway node in the patch. To provide redundancy in the transit network, multiple micro-solar router nodes cover a 120 m stretch from a shed housing the gateway across an old apple orchard. These nodes are just patch nodes without the environmental sensors. The network depth is five hops or greater. The IEEE 802.15.4 bridge node attached to the base station uses a high-gain (19 dBi) parabolic antenna pointed out through a window in the shed. The back haul network is a WiFi-based IP network with repeaters on peaks and tree tops to

[8]Sentilla Tmote Sky. `http://www.sentilla.com/pdf/eol/tmote-sky-datasheet.pdf`.

[9]Primer Pack/IP. `http://archrock.com/downloads/datasheet/primerpack_datasheet.pdf`.

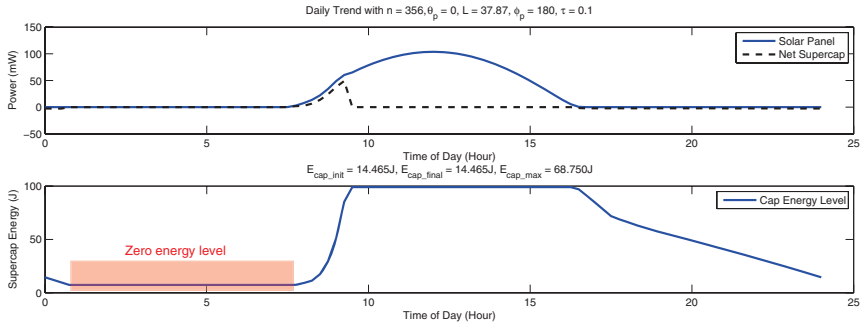

(a) 22F supercapacitor, $I_{load} = 0.53mA$.

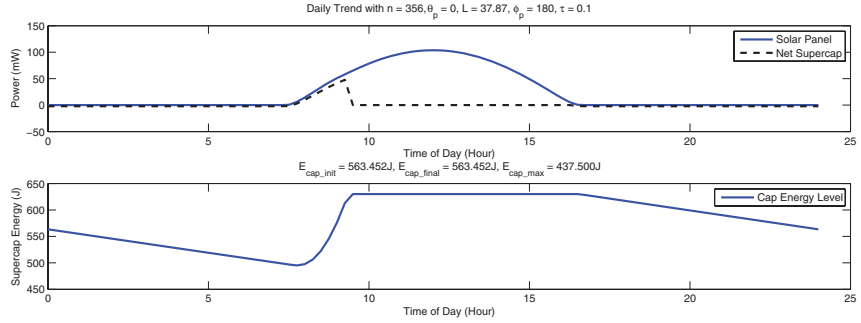

(b) 140F supercapacitor, $I_{load} = 0.53mA$.

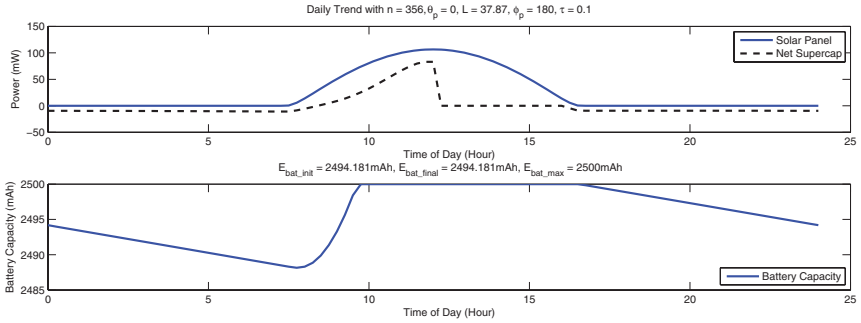

(c) Two 2500mAh NiMH batteries, $I_{load} = 0.53mA$.

Energy Storage	**One 22F supercap**	**One 140F supercap**	**Two 2500mAh NiMH batteries**
Load current I_{load}	0.53 mA	0.53 mA	0.53 mA
Charging time T_c	2 hour	2 hour	2 hour 15 minutes
Discharging time T_d	8 hour 15 minutes	14 hour 45 minutes	14 hour 45 minutes
Discharged energy E_d	91.685J	134.836J	11.852mAh (= 119.465J at 2.8V)

Fig. 21. A micro-solar power system under worst-case yearly solar radiation with HydroWatch workload (day of year $n = 356$). 4.0V-100mA solar panel, MAX1724 step-up DC-DC converter (output regulator), TelosB node (load) and no input regulator was used.

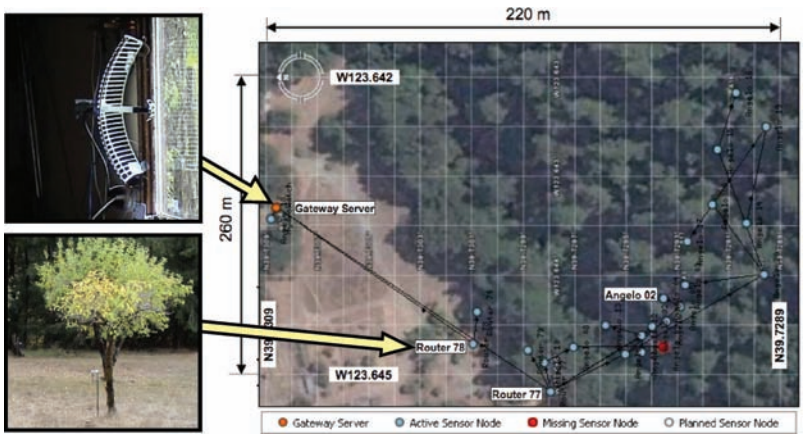

Fig. 22. Snapshot of the HydroWatch forest watershed deployment.

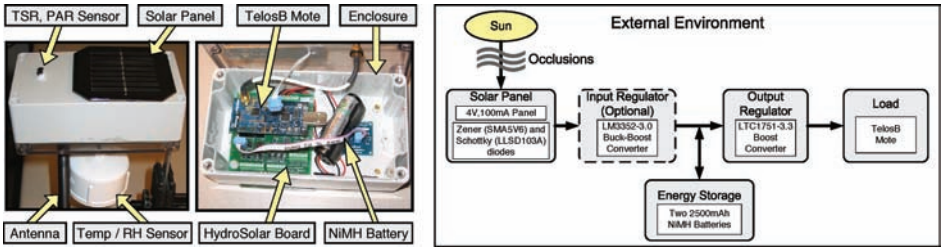

Fig. 23. HydroWatch weather node and its micro-solar power subsystem.

reach a T1 line. The base station is a Linux-class gateway server that provides a Web services frontend, a PostgreSQL database for information storage and retrieval, and a Web-based management console.

5.1.2. Micro-Solar Power Subsystem of HydroWatch Node. The core of the node design is a flexible power subsystem board that ties together a solar panel, an optional input regulator, a battery, and a switching output regulator, as shown in Figure 23. It provides measurement points for a number of electrical parameters that can be connected to the mote ADCs, sampled, and recorded along with the environmental measurements. In our configuration, these monitoring features produce time-series logs of solar panel voltage, solar panel current, and battery voltage, in addition to the logs of sensor data from the application and link/neighbor data. All of these are collected and stored by the gateway server, enabling deeper analysis of the performance of the node and network under varying solar conditions. The solar board also provides the mechanical structure that attaches the mote to the enclosure. The HydroWatch board was designed to permit the study of a variety of power subsystem options. The solar panel and the battery are attached through screw terminals. Headers and mounting holes permit direct attachment of motes of the TelosB form factor, but a mote of any other type can be attached to the board through screw terminals. Additionally, the board has a prototyping area which can be used to change power subsystem configuration. In fact, we were able to change any of the circuit elements originally used in the board schematic by simply changing jumper settings and populating the prototyping area. We used this flexibility to evaluate candidate parts for each component and quantify

Table III. Components for the HydroWatch Board

(a) Solar Panel (Silicon Solar #16530)	
V_{oc} , I_{sc}	4.23V, 111.16mA
MPP	276.0mW at 3.11V
I-V curve	Shown in Figure 11
Dimension	2.3in x 2.3in
Material, Efficiency	Polycrystalline silicon, 13%
(b) Input Regulator (LM3352-3.0: Optional)	
Manufacturer-provided efficiency	65%-83% (I_{out} = 5mA-100mA, V_{out} = 3.0V, V_{in} = 2.5V-3V)
Measured efficiency	54.71%-65.40% (I_{solar} = 0mA-100mA, V_{out} = 3.0V)
(c) Energy Storage	
Configuration	Two AA NiMH batteries in series
Voltage	2.4V nominal, 2.6V-3.0V at charge
Capacity	2 × 1.2V × 2500mAh = 6000mWh
(d) Output Regulator (LTC1751-3.3)	
Manufacturer-provided efficiency	55%-60% (I_{out}=0.1mA-20mA, V_{in}=2.75V, V_{out}=3.3V)
Measured efficiency	49.69%-52.15% (I_{out}=3mA-6mA, V_{in}=2.55V-2.71V, V_{out}=3.3V)
(e) Load	
Mote platform	Tmote Sky / TelosB mote
Vcc	2.1V - 3.6V, 2.7V - 3.6V with flash
Average current	App.-Dependent; 0.53mA for ours
Maximum current	23mA with MCU on, radio RX

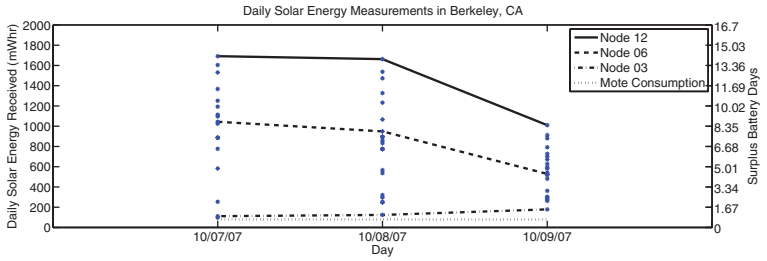

Fig. 24. Scatter plot of solar energy received in the urban neighborhood deployment from October 7, 2007 to October 9, 2007. Three representative nodes are highlighted.

their contribution to the efficiency of the entire system. The components selected for the HydroWatch micro-solar board are summarized in Table III.

5.2. Evaluating the Reference Implementation

5.2.1. A Sensor Network in an Urban Neighborhood. The purpose of our first deployment was to confirm that nodes could sense, charge, and operate continuously for a period of days, as well as assess whether the model we developed accurately estimated the generation and consumption of energy in a variety of solar conditions. We deployed 22 nodes in an urban neighborhood in Berkeley; nodes were placed in varied locations, including on a house gutter, in and under trees, among shrubbery, and in a grassy yard. To emulate the situation in the forest watershed, we placed them in the vicinity of significant obstructions and varied the orientation of the solar panels: some were flat while others faced south, east, and west at a 45 degree inclination.

The range of daily solar energy via P_{sol} by each node over a period of three days can be seen in Figure 24. The lines on the graph show the behavior of the node that received the highest (Node 12), median (Node 06), and lowest (Node 03) amount of solar energy. The fourth line on the graph shows a constant 79.2 mWh break-even point. The first day (October 7, 2007) was a fairly sunny day, resulting in the widest distribution of received

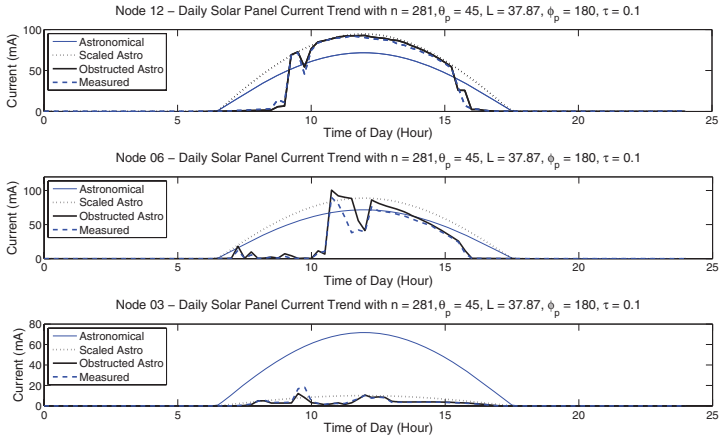

Fig. 25. Comparison of solar panel output current on a sunny day (Oct. 8, 2007) for the best, middle, and worst mode in the urban neighborhood deployment. Notice the differences in scale of the graphs.

solar energy (roughly 100–1700 mWh). However, as the days became cloudier, the variance of the distribution lessened; nodes at the high end of the distribution received slightly more than half the solar energy when the day was cloudy, compared to a sunny day. Interestingly, nodes on the lower end of the distribution received more solar energy on cloudier days; this is presumably because the diffusion of light caused by the layer of clouds scatters the light source and enhances the opportunity of the normally occluded solar panel to harvest solar energy. Nonetheless, every node harvests a surplus of energy on both sunny and cloudy days; the number of surplus battery days this energy creates is also in Figure 24. Surplus battery days are calculated by multiplying the surplus of energy flowing into the battery by the charge-discharge efficiency (66%) and dividing by the daily consumption (79.2 mWh).

Looking at the daily graph of solar current experienced at each of the three representative nodes on a sunny day (shown in Figure 25), we can see the variations in available solar energy inputs among nodes throughout a day. Additionally, these current graphs are plotted alongside the three estimation models (astronomical, scaled astronomical, and obstructed astronomical) as a basis for comparison. In this experiment, scaled astronomical and obstructed astronomical models were trained from the one-day measurement on October 7, 2007, because we were able to observe a clear weather condition. The measurement of the solar profile fits the astronomical model when the solar panel has an unobstructed view of sunlight for a certain period of time. For other cases, whether the solar panel is obstructed during part of the day (Node 12 and Node 06) or the whole day (Node 03), the estimation from the astronomical model deviates far from the measurement. The obstructed astronomical model captures the shading effect and gives a better fitting to the measurement than the astronomical model. On an overcast day, (see Figure 26) the gap between the measurement and the estimation of each model becomes higher because the estimation models capture time variation and obstruction effects, but not the weather effects. Table IV summarizes the solar panel output energy measurement and estimations for both a sunny day (October 8, 2007) and an overcast day (October 9, 2007). We can see that the astronomical model has a higher estimation error, as the node is obstructed for longer hours, whereas the obstructed astronomical model fits the measurement on any obstruction conditions.

The urban neighborhood deployment demonstrated that even nodes with severe arboreal and other occlusions received enough sunlight to sustain operation, that is,

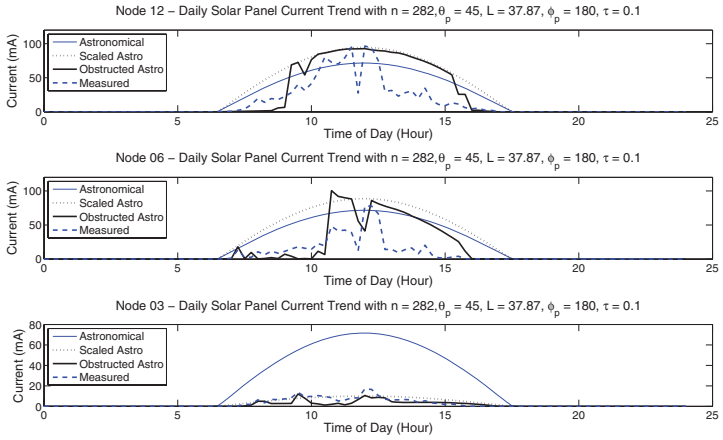

Fig. 26. Comparison of solar panel output current on an overcast day (Oct. 9, 2007) for the urban neighborhood deployment.

Table IV. Daily Solar Panel Output Energy for Different Estimation Models

(a) Node with highest solar radiation (Node 12)

	Astronomical	Scaled Astro	Obstructed Astro	Measurement
Oct. 8, 2007	1691.2 mWh	2217.6 mWh	1721.8 mWh	1649.7 mWh
Oct. 9, 2007	1691.2 mWh	2217.6 mWh	1721.7 mWh	1034.5 mWh

(b) Node with median solar radiation (Node 06)

	Astronomical	Scaled Astro	Obstructed Astro	Measurement
Oct. 8, 2007	1691.2 mWh	2079.1 mWh	1137.7 mWh	946.1 mWh
Oct. 9, 2007	1691.2 mWh	2079.1 mWh	1137.7 mWh	561.9 mWh

(c) Node with lowest solar radiation (Node 03)

	Astronomical	Scaled Astro	Obstructed Astro	Measurement
Oct. 8, 2007	1691.2 mWh	235.0 mWh	127.0 mWh	126.9 mWh
Oct. 9, 2007	1691.2 mWh	235.0 mWh	127.1 mWh	173.7 mWh

Note: Deployment was in an urban neighborhood on a sunny day (Oct. 8, 2007) and an overcast day (Oct. 9, 2007).

the nodes in the most shade still received at least 30 minutes of sunlight on both sunny and cloudy days, validating the prediction of our model and making us (falsely) confident that our design would succeed in the forest watershed.

5.2.2. A Sensor Network in a Forest Watershed. The blend of solar profiles seen by the nodes in the forest watershed was far less diverse than the urban neighborhood, as shown in Figure 27. Most of the nodes received no more than 50 mWh of energy on any of the days of the deployment. Just as in Figure 24, the lines represent nodes chosen to show the range of the solar distribution. However, in Figure 27, the middle line represents the second-best performing node (not the median), and the lowest line is for a node representative of those that are receiving very limited energy. The stunning difference between the two deployments is how much less solar energy was harvested in the forest watershed—the best-performing node on a sunny day in the forest did not receive as much solar energy as the median node on a cloudy day in the urban neighborhood. Additionally, Angelo 02 (and other sun-starved nodes like it) harvested less than the node consumption each day. This daily energy deficit results in a negative number of surplus battery days. It is important to note that these nodes are experiencing different degrees of sun starvation—some are only consuming about half a day's worth of battery energy daily, while others are consuming a full day's worth of energy. Still, a majority

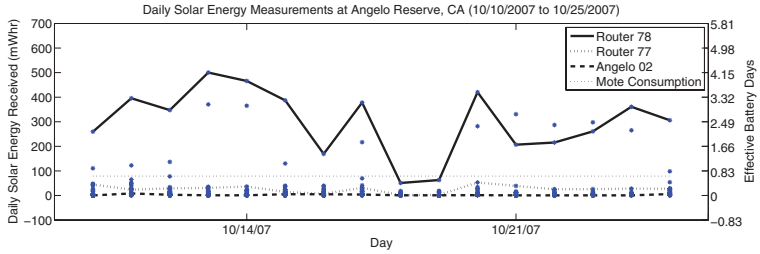

Fig. 27. Scatter plot of solar energy received in the forest watershed deployment from Oct. 10, 2007 to Oct. 25, 2007. Three representative nodes are highlighted. Note that the daily averages of mote consumption are represented as a single line in the graph because they had nearly the same values over time.

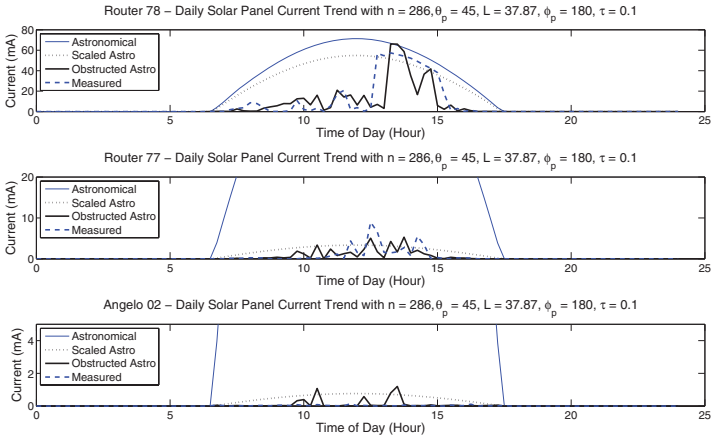

Fig. 28. Comparison of solar panel current on a sunny day (Oct. 13, 2007) in the forest watershed deployment. Notice the differences in the scale of the graphs.

of the nodes were not receiving sufficient solar energy to operate sustainably, causing a finite lifetime for the network.

Figures 28 and 29 show the solar current of the three representative nodes on a sunny and overcast day, respectively. The solar currents noticeably suffer on the overcast day, but the heavily shaded node slightly improves its energy harvesting. Perhaps the most important observation is how spiky the solar profile is for the nodes that receive reasonable amounts of solar energy.

Figure 30 shows the trends of solar radiation for the three representative nodes. In this forest deployment, most nodes are heavily occluded, and the astronomical model, which assumes unobstructed view of the sky, does not effectively estimate the solar radiation, with an estimation error of 80.9% to 99.9%. The obstructed astronomical model fits the measurement within around 30% of error for nodes with high radiation condition (Router 78) and medium radiation condition (Router 77). This 30% difference is due to two factors: variations in external conditions, such as a weather effect, and inherent limitation with our model (e.g., no consideration of temperature variation). For the low-exposure node (Angelo 02), the effect of these factors becomes more important with the estimation error of 68%.

5.3. Predicting the Long-Term Behavior

Urban neighborhood and forest watershed deployments in Section 5.2 showed that the obstructed astronomical model could estimate solar radiation with a modest amount

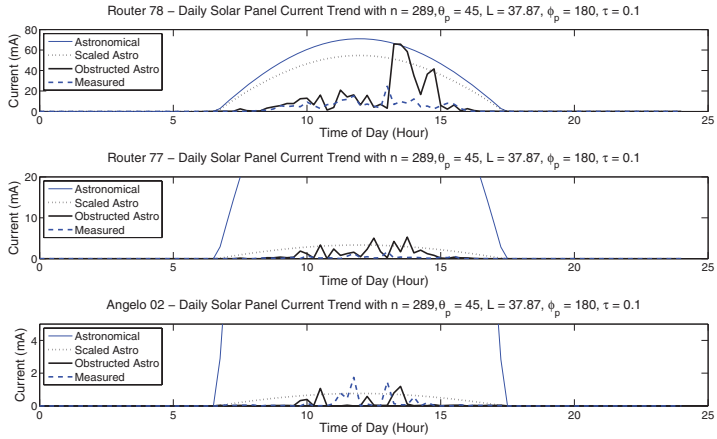

Fig. 29. Comparison of solar panel current on an overcast day (Oct. 16, 2007) in the forest watershed deployment. Notice the differences in the scale of the graphs.

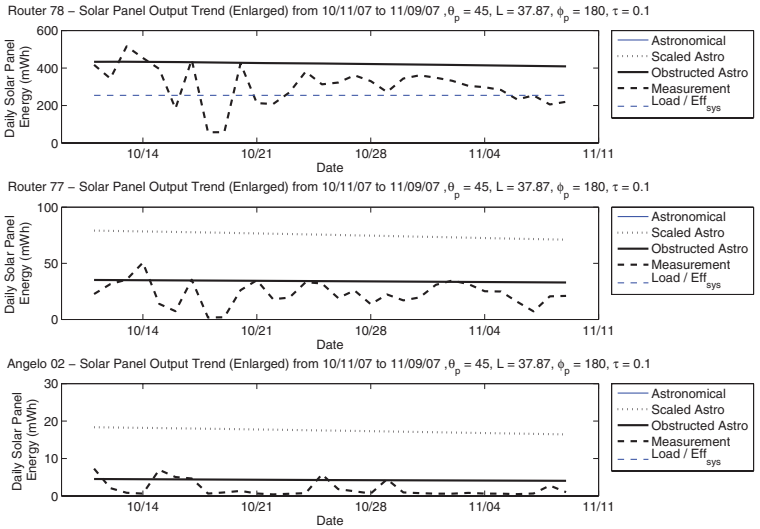

Deviation from measurement	Astronomical	Scaled Astro	Obstructed Astro
Router 78	80.9%	75.4%	29.8%
Router 77	98.6%	69.3%	35.8%
Angelo 02	99.9%	89.3%	68.3%

Fig. 30. Comparison of different radiation estimation methods on forest deployment over the measurements from Oct. 11, 2007 to Nov. 9, 2007.

of error; however, they are limited in that measurements were taken over a relatively short period of time. In this section, we demonstrate how our model estimates solar radiation in the presence of seasonal and weather variations using a long-term measurement of HydroWatch weather nodes. In order to see the effect of weather variations, we deployed five HydroWatch weather nodes on the rooftop of the Valley Life Science Building (VLSB) at UC Berkeley where micro-solar nodes can get solar radiation without any obstructions from trees or other buildings (Figure 31). Since there are no obstructions between each node and the sun, the measurement of the solar panel

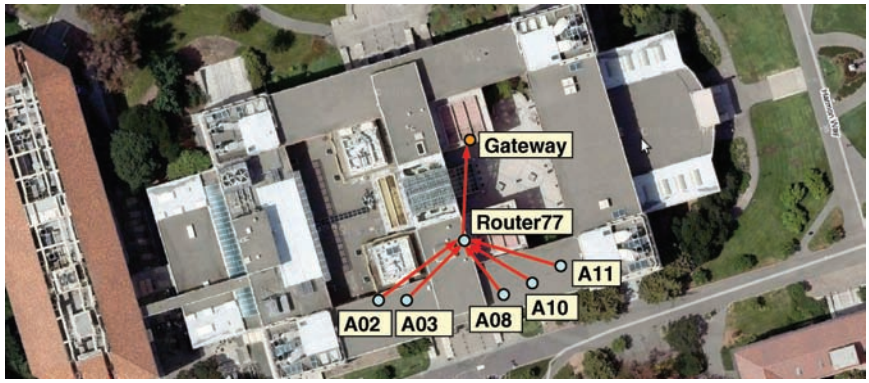

Fig. 31. Deployment map of HydroWatch nodes on the rooftop of the Valley Life Science Building at UC Berkeley. The experiment was conducted from Dec. 22, 2007 (n = 356) to Apr. 15, 2008 (n = 365 + 106) at Berkeley, CA (37.87°N). As for solar panel inclination θ_p and orientation ϕ_p, nodes A02 and A08 had their panels tilted 45° ($\theta_p = 45$) facing south ($\phi_p = 180$), and nodes A03, A10, and A11 had their panels flat to the ground ($\theta_p = 0$).

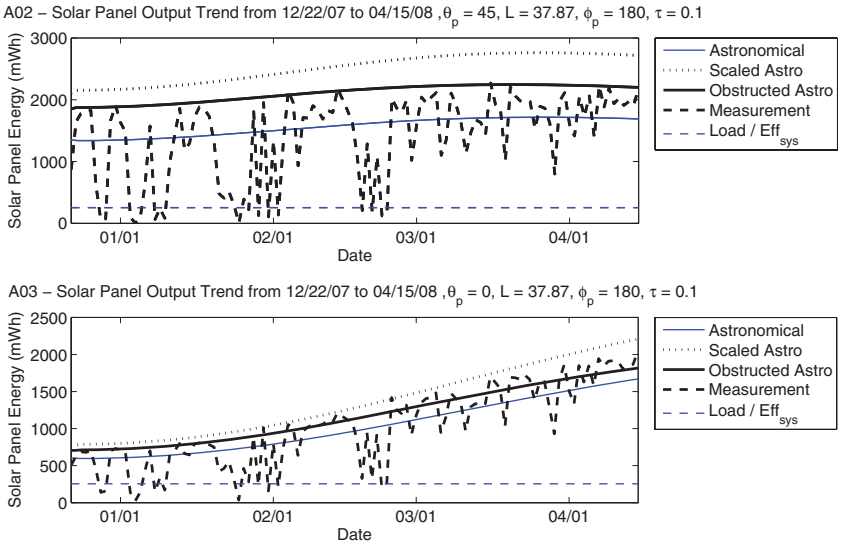

Fig. 32. Seasonal solar radiation variation of HydroWatch weather nodes on the rooftop of the Valley Life Science building at UC Berkeley from Dec. 22, 2007 to Apr. 15, 2008.

output depends only on the diurnal and seasonal variation of solar radiation and the weather variation. The astronomical model gives an estimation of diurnal and seasonal variation of the solar radiation. We use the obstructed astronomical model in order to fit the astronomical model to the measurement, then we account for the weather effect by comparing the solar panel output measurement with the prediction from the obstructed astronomical model. Figure 32 compares the daily solar panel energy measurement with a few estimation models. From this plot, we can observe the following.

—*Seasonal Variation*. The three estimation models (astronomical, scaled astronomical, and obstructed astronomical) capture the seasonal variation well, and the obstructed astronomical model tracks the peak of the measurement.

Table V. Deviation of the Obstructed Astronomical Model from the Measurement

	A02	A03	A08	A10	A11
Deviation	34.0%	23.2%	31.4%	26.7%	31.1%

Table VI. Correlation Coefficient for the Weather Trend in VLSB Deployment

	A02	A03	A08	A10	A11
A02	1.0	0.97073	0.97644	0.98154	0.98055
A03		1.0	0.95558	0.99355	0.99114
A08			1.0	0.96877	0.95503
A10				1.0	0.99244
A11					1.0

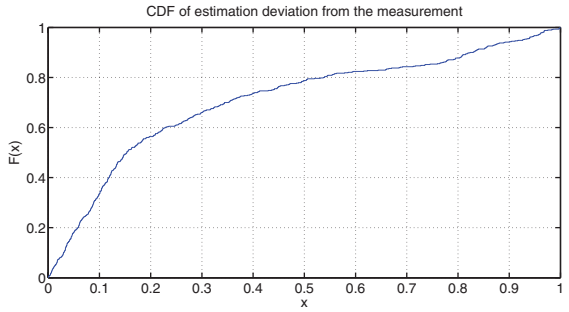

Fig. 33. Cumulative distribution function (CDF) of the estimation deviation from the measurement for the obstructed astronomical model.

—*Weather Effect*. The obstructed astronomical model deviates from the measurement within about 30% due to weather.

In order to see whether this weather effect is only for these particular nodes or for all the nodes in the deployment, we did the following analysis for all the nodes. First, we calculated the deviation of the obstructed astronomical model $DV(n,t)$ as a relative difference between the estimation $AST(n,t)$ and the measurement $M(n,t)$: $DV(n,t) = (AST(n,t) - M(n,t))/AST(n,t)$. The average of the deviation for all the nodes are shown in Table V. We can see that there is slight variation, but the deviation of the estimation from the measurement is about 30%. Second, we calculated the correlation coefficient of the deviation for all the two pairs of the nodes in the deployment (Table VI). The correlation coefficient is between 95% to 99%, and this implies that all the nodes in the deployment experienced the same weather variation. Figure 33 shows the distribution of the deviation of the obstructed astronomical model to the measurement. This distribution has 0.29 as its average. We can also see that about half of the deviations are within 0.15, and the other half has a long tail and is spread from 0.15 to 1. This distribution implies that much of the solar radiation measurement deviates within a small fraction of the estimate, but a non-negligible amount of measurement deviates a large fraction of the estimate.

6. CONCLUDING REMARKS

In this article, we have presented a practical theory that enables a systematic design of a micro-solar power system. We summarize this article as follows. First, we have developed a general model of micro-solar power systems. It consists of several lumped elements, such as the external environment, a solar collector, an input regulator, energy storage, output regulator, and a load, and their relationship in terms of

energy flow and efficiency factors. In this framework, designing a micro-solar power system implies setting the parameters of one or more of these lumped elements. Second, we have materialized this model into a simulation suite by formulating each component of a micro-solar power system into an analytical module and composing these modules into an instance of a micro-solar power system. In order to represent the external environment, we have proposed two methods: an astronomical model and an obstructed astronomical model. The astronomical model estimates solar radiation using well known formulas without any knowledge of the deployment site. The obstructed astronomical model refines the estimates of the astronomical model using a few samples of local measurements, incurring a modest estimation error. Using all of these components, we have composed a few instances of micro-solar power systems. Using benchtop experiments, we have shown that these simulation tools work in a small time frame. Third, we have implemented a reference platform of a micro-solar power system, the HydroWatch node, and validated the simulation suite by comparing solar energy estimates with empirical results in a realistic environment. The deployment, where reference platform nodes were placed under varying solar profiles in urban neighborhoods and forest watershed environments, showed that our simulation tools could estimate the solar energy budget with a small degree of error.

We have shown that our simulation tools can predict the solar profile well and that it is possible to design a micro-solar power system for long-term survival, but we have some ideas for improving accuracy and generality. For improving prediction accuracy, we plan to design a weather effect model which predicts solar radiation variation due to weather effects using recent history of weather effects, such as horizontal visibility and cloud cover. For supporting various types of micro-solar power systems, we plan to write simulation components for maximum power point tracking and multilevel energy storage. For supporting a solar power system of larger scale, we plan to write simulation components for macro- or meso-solar systems and demonstrate that our simulation tools can be used irrespective of the scale of a system. Finally, we plan to extend our simulation tools to other types of renewable energy sources, such as wind and vibrations.

REFERENCES

Castaner, L. and Silvestre, S. 2002. *Modeling Photovoltaic Systems Using PSpice*. John Wiley & Sons, Huboken, NJ.

Corke, P., Valencia, P., Sikka, P., Wark, T., and Overs, L. 2007. Long-duration solar-powered wireless sensor networks. In *Proceedings of the 4th IEEE Workshop on Embedded Networked Sensors (EmNets'07)*.

Dave, J. V., Halpern, P., and Myers, H. J. 1975. Computation of incident solar energy. *IBM J. Res. Develop. 19,* 6, 539–549.

Dubayah, R. and Rich, P. M. 1995. Topographic solar radiation models for gis. *Int. J. Geog. Inf. Sci. 9,* 4, 405–419.

Dunkels, A., Osterlind, F., Tsiftes, N., and He, Z. 2007. Software-based on-line energy estimation for sensor nodes. In *Proceedings of the 4th IEEE Workshop on Embedded Networked Sensors (EmNets'07)*.

Dutta, P., Hui, J., Jeong, J., Kim, S., Sharp, C., Taneja, J., Tolle, G., Whitehouse, K., and Culler, D. 2006. Trio: Enabling sustainable and scalable outdoor wireless sensor network deployments. In *Proceedings of the 5th International Conference on Information Processing in Sensor Networks (IPSN/SPOTS'06)*.

Fonseca, R., Dutta, P., Levis, P., and Stoica, I. 2008. Quanto: Tracking energy in networked embedded systems. In *Proceedings of the 8th USENIX Symposium on Operating System Design and Implementation (OSDI'08)*.

Handziski, V., Köpke, A., Willig, A., and Wolisz, A. 2006. Twist: A scalable and reconfigurable testbed for wireless indoor experiments with sensor networks. In *Proceedings of the 2nd International Workshop on Multi-Hop Ad Hoc Networks: From Theory to Reality (REALMAN'06)*.

Ingelrest, F., Barrenetxea, G., Schaefer, G., Vetterli, M., Couach, O., and Parlange, M. 2010. Sensorscope: Application-specific sensor network for environmental monitoring. *ACM Trans. Sens. Netw.*

JIANG, X., POLASTRE, J., AND CULLER, D. 2005. Perpetual environmentally powered sensor networks. In *Proceedings of the 4th International Symposium on Information Processing in Sensor Networks (IPSN/SPOTS'05)*.

KANSAL, A., HSU, J., ZAHEDI, S., AND SRIVASTAVA, M. B. 2007. Power management in energy harvesting sensor networks. *ACM Trans. Embed. Compu. Syst*.

KANSAL, A., POTTER, D., AND SRIVASTAVA, M. B. 2004. Performance aware tasking for environmentally powered sensor networks. In *Proceedings of the Joint International Conference on Measurement and Modeling of Computer Systems (SIGMETRICS)*.

KIM, S. 2007. Wireless sensor networks for high frequency sampling. Ph.D dissertation, University of California at Berkeley.

LANDSIEDEL, O., WEHRLE, K., AND GÖTZ, S. 2005. Accurate prediction of power consumption in sensor networks. In *Proceedings of the 2nd IEEE Workshop on Embedded Networked Sensors (EmNets'05)*.

LI, D. AND CHOU, P. H. 2004. Maximizing efficiency of solar-powered systems by load matching. In *Proceedings of the International Symposium on Low Power Electronics and Design (ISLPED)*.

MADDEN, S., FRANKLIN, M. J., HELLERSTEIN, J. M., AND HONG, W. 2002. Tag: A tiny aggregation service for ad-hoc sensor networks. In *Proceedings of the 5th Symposium on Operating Systems Design and Implementation (OSDI'02)*.

MONTENEGRO, G., KUSHALNAGAR, N., HUI, J., AND CULLER, D. 2007. Transmission of ipv6 packets over ieee 802.15.4 networks. http://tools.ietf.org/html/rfc4944.

MOSER, C., BRUNELLI, B., THIELE, L., AND BENINI, L. 2006a. Lazy scheduling for energy harvesting sensor nodes. In *Proceedings of the IFIP Conference on Model-Driven Design to Resource Management for Distributed Embedded Systems*.

MOSER, C., BRUNELLI, B., THIELE, L., AND BENINI, L. 2006b. Real-time scheduling with regenerative energy. In *Proceedings of the 18th Euromicro Conference on Real-Time Systems (ECRTS'06)*.

NATH, S., GIBBONS, P. B., SESHAN, S., AND ANDERSON, Z. R. 2004. Synopsis diffusion for robust aggregation in sensor networks. In *Proceedings of the 2nd ACM Conference on Embedded Networked Sensor Systems (Sensys'04)*.

NEWTON, A. R. 1978. The simulation of large scale integrated circuits. Ph.D dissertation, University of California at Berkeley.

PARADISO, J. A. 2006. Systems for human-powered mobile computing. In *Proceedings of the IEEE Design Automation Conference (DAC)*.

PARK, C. AND CHOU, P. H. 2006. Ambimax: Autonomous energy harvesting platform for multi-supply wireless sensor nodes. In *Proceedings of the IEEE International Conference on Sensing, Communication and Networking (SECON)*.

PARK, S., SAVVIDES, A., AND SRIVASTAVA, M. B. 2000. Sensorsim: A simulation framework for sensor networks. In *Proceedings of the International Workshop on Modeling Analysis and Simulation of Wireless and Mobile Systems (MSWIM)*.

PARK, S., SAVVIDES, A., AND SRIVASTAVA, M. B. 2001. Simulating networks of wireless sensors. In *Proceedings of the Winter Simulation Conference*.

POLASTRE, J., HILL, J., AND CULLER, D. 2004. Versatile low power media access for wireless sensor networks. In *Proceedings of the 2nd ACM Conference on Embedded Networked Sensor Systems (Sensys'04)*.

POLASTRE, J., SZEWCZYK, R., AND CULLER, D. 2005. Telos: Enabling ultra-low power wireless research. In *Proceedings of the 4th International Symposium on Information Processing in Sensor Networks (IPSN/SPOTS'05)*.

POP, V., BERGVELD, H. J., NOTTEN, P. H. L., AND REGTIEN, P. P. L. 2005. State-of-the-art of battery state-of-charge determination. *Ins. Physics Publish. Meas. Sci. Techno.*

PRADHAN, S. S., KUSUMA, J., AND RAMCHANDRAN, K. 2002. Distributed compression in a dense microsensor network. *IEEE Signal Proces. Mag.*

RAGHUNATHAN, V., KANSAL, A., HSU, J., FRIEDMAN, J., AND SRIVASTAVA, M. 2005. Design considerations for solar energy harvesting wireless embedded systems. In *Proceedings of the 4th International Symposium on Information Processing in Sensor Networks (IPSN/SPOTS'05)*.

RANDALL, J. F. 2005. *Designing Indoor Solar Products, Photovoltaic Technologies for AES*. John Wiley & Sons, Hoboken, NJ.

RAO, R., VRUDHULA, S., AND RAKHMATOV, D. N. 2003. Battery modeling for energy-aware system design. *IEEE Comput.*

ROUNDY, S., OTIS, B. P., CHEE, Y.-H., RABAEY, J. M., AND WRIGHT, P. 2003. A 1.9ghz rf transmit beacon using environmentally scavenged energy. In *Proceedings of the International Symposium on Low Power Electronics and Design (ISLPED)*.

ROUNDY, S. J. 2003. Energy scavenging for wireless sensor nodes with a focus on vibration to electricity conversion. Ph.D. dissertation, University of California at Berkeley.

SHNAYDER, V., HEMPSTEAD, M., CHEN, B., WERNER-ALLEN, G., AND WELSH, M. 2004. Simulating the power consumption of large-scale sensor network applications. In *Proceedings of the 2nd ACM Conference on Embedded Networked Sensor Systems (Sensys'04)*.

SIKKA, P., CORKE, P., VALENCIA, P., CROSSMAN, C., SWAIN, D., AND BISHOP-HURLEY, G. 2006. Wireless adhoc sensor and actuator networks on the farm. In *Proceedings of the 5th International Conference on Information Processing in Sensor Networks (IPSN/SPOTS'06)*.

SIMJEE, F. AND CHOU, P. H. 2006. Everlast: Long-life, supercapacitor-operated wireless sensor node. In *Proceedings of the International Symposium on Low Power Electronics and Design (ISLPED)*.

SIMON, G., VOLGYESI, P., MAROTI, M., AND LEDECZI, A. 2003. Simulation-based optimization of communication protocols for large-scale wireless sensor networks. In *Proceedings of the IEEE Aerospace Conference*.

SOBER, J., KOSTADINOV, A., GARBER, M., BRENNAN, M., CORNER, M. D., AND BERGER, E. D. 2007. Eon: A language and runtime system for perpetual systems. In *Proceedings of the 5th ACM Conference on Embedded Networked Sensor Systems (Sensys'07)*.

SUNDRESH, S., KIM, W., AND AGHA, G. 2004. Sens: A sensor, environment and network simulator. In *Proceedings of the 37th Annual Simulation Symposium (ANSS'04)*.

SZEWCZYK, R., MAINWARING, A., POLASTRE, J., ANDERSON, J., AND CULLER, D. 2004. An analysis of a large scale habitat monitoring application. In *Proceedings of the 2nd ACM Conference on Embedded Networked Sensor Systems (Sensys'04)*.

TANEJA, J., JEONG, J., AND CULLER, D. 2008. Design, modeling, and capacity planning for micro-solar power sensor networks. In *Proceedings of the 7th International Conference on Information Processing in Sensor Networks (IPSN/SPOTS'08)*.

TOVAR-PESCADOR, J., POZO-VÁZQUEZ, D., RUIZ-ARIAS, J. A., BATLLES, J., LÓPEZ, G., AND BOSCH, J. L. 2006. On the use of the digital elevation model to estimate the solar radiation in areas of complex topography. *Meteorol. Appl.*, 297–287.

VARSHNEY, M., XU, D., SRIVASTAVA, M., AND BAGRODIA, R. 2007. squalnet: A scalable simulation and emulation environment for sensor networks. In *Proceedings of the 7th International Conference on Information Processing in Sensor Networks (IPSN/SPOTS'07)*.

VIGORITO, C. M., GANESAN, D., AND BARTO, A. G. 2007. Adaptive control of duty cycling in energy-harvesting wireless sensor networks. In *Proceedings of the IEEE International Conference on Sensing Communications, and Networking (SECON)*.

WERNER-ALLEN, G., SWIESKOWSKI, P., AND WELSH, M. 2005. Motelab: A wireless sensor network testbed. In *Proceedings of the 4th International Symposium on Information Processing in Sensor Networks (IPSN/SPOTS'05)*.

YE, W., HEIDEMANN, J., AND ESTRIN, D. 2004. Medium access control with coordinated adaptive sleeping for wireless sensor networks. *IEEE/ACM Trans. Netw. 3*.

YE, W., SILVA, F., AND HEIDEMANN, J. 2006. Ultra-low duty cycle mac with scheduled channel polling. In *Proceedings of the 4th ACM Conference on Embedded Networked Sensor Systems (Sensys'06)*.

ZHANG, P., SADLER, C. M., LYON, S. A., AND MARTONOSI, M. 2004. Hardware design experiences in zebranet. In *Proceedings of the 2nd ACM Conference on Embedded Networked Sensor Systems (Sensys'04)*.

Received January 2009; revised August 2010, September 2011; accepted November 2011